Physical Properties of Morphological Units on Comet 9P/Tempel 1 Derived from Near–IR Deep Impact Spectra

Björn J.R. Davidsson, Pedro J. Gutiérrez, Hans Rickman

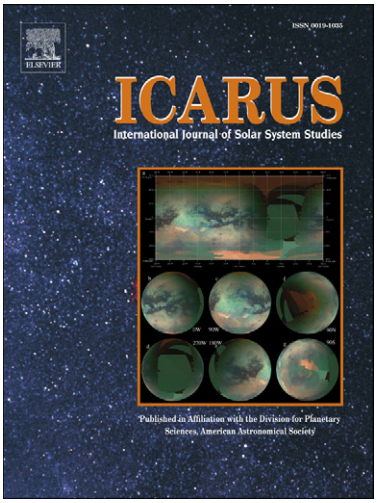

Physical Properties of Morphological Units on Comet 9P/Tempel 1 Derived from Near–IR Deep Impact Spectra

Björn J.R. Davidsson, Pedro J. Gutiérrez, Hans Rickman

PII: S0019-1035(09)00002-5
DOI: 10.1016/j.icarus.2008.12.039
Reference: YICAR 8869

To appear in: *Icarus*

Received date: 14 August 2008
Revised date: 17 December 2008
Accepted date: 29 December 2008

Please cite this article as: B.J.R. Davidsson, P.J. Gutiérrez, H. Rickman, Physical Properties of Morphological Units on Comet 9P/Tempel 1 Derived from Near–IR Deep Impact Spectra, *Icarus* (2009), doi: 10.1016/j.icarus.2008.12.039

Title: Physical Properties of Morphological Units on Comet 9P/Tempel 1 Derived from Near–IR Deep Impact Spectra

Author (1): Björn J. R. Davidsson

Affiliation: Department of Physics and Astronomy, Uppsala University

Address: Box 515, SE–75120 Uppsala, Sweden.

Telephone: +46–(0)18–4715970

Fax number: +46–(0)18–4715999

E–mail address: bjorn.davidsson@fysast.uu.se

Author (2): Pedro J. Gutiérrez

Affiliation: Instituto de Astrofísica de Andalucía–CSIC

Address: Aptd 3004, 18080 Granada, Spain.

Telephone: +34–958–121311

Fax number: +34–958–814530

E–mail address: pedroj@iaa.es

Author (3): Hans Rickman

Affiliation (1): Department of Physics and Astronomy, Uppsala University

Address (1): Box 515, SE–75120 Uppsala, Sweden.

Telephone (1): +46–(0)18–4715971

Fax number (1): +46–(0)18–4715999

E–mail address: hans.rickman@fysast.uu.se

Affiliation (2): PAN Space Research Center

Address (2): Bartycká 18A, PL–00716 Warsaw, Poland.

Telephone (2): +48–(0)22–8403766

Fax number (2): +48–(0)22–8403131

E–mail address: hans.rickman@fysast.uu.se

Number of manuscript pages: 74

Number of figures: 12

Number of tables: 2

Running head: Physical Properties of Morphological Units on Comet 9P/Tempel 1

Address for editorial correspondence:

Björn Davidsson

Department of Physics and Astronomy

(Delivery address: Regementsvägen 1)

Box 515

SE–75120 Uppsala

Sweden

Email: bjorn.davidsson@fysast.uu.se

+46–(0)18–4715970 (phone)

+46–(0)18–4715999 (fax)

Abstract

In this paper we analyze near–infrared thermal emission spectra of the spatially resolved nucleus of Comet 9P/Tempel 1 obtained by the NASA spacecraft *Deep Impact*. Maps of spectral reddening, the product X' between the beaming function and directional emissivity, as well as surface temperature are constructed. Thermophysical modeling is used to estimate the degree of small scale surface roughness and thermal inertia by detailed reproduction of the empirical temperature map. Mie and Hapke theories are used in combination with numerically calculated beaming functions to analyze the X' map and place constraints on composition and grain size of the surface material.

We show that it is absolutely mandatory to include small scale surface roughness in thermophysical modeling of this object, since the resulting self heating is vital for reproducing the measured temperatures. A small scale self heating parameter in the range $0.6 \leq \xi \leq 0.75$ is common, but smoother areas where $0.2 \leq \xi \leq 0.3$ are also found. Contrary to models neglecting small scale surface roughness, we find that the thermal inertia of Comet 9P/Tempel 1 generally is high (1000–3000 $\mathrm{J\,m^{-2}\,K^{-1}\,s^{-1/2}}$), although it may be substantially lower (40–380 $\mathrm{J\,m^{-2}\,K^{-1}\,s^{-1/2}}$) in specific areas. We obtain a disk–averaged reddening of $3.5\,\%\,\mathrm{k\AA^{-1}}$, with statistically significant local variations around that value on a $\pm 1.0\,\%\,\mathrm{k\AA^{-1}}$ level. Vast regions appear covered by small ($\sim 0.1\,\mu$m) highly absorbing grains such as carbon or iron–rich silicates. Other regions appear dominated by somewhat larger ($\sim 0.5\,\mu$m) and/or less absorbing grains such as troilite or magnesium–rich silicates.

Surface variations in reddening, roughness, thermal inertia, composition and/or grain size are moderately to strongly correlated to the locations of morphological units on the surface. The existence of morphological units with differing physical properties may be primordial, hence reflecting a diversity in the building block cometesimals, or resulting from evolutionary processes.

Key Words: Comet 9P/Tempel 1; Comets, Nucleus; Thermal Histories; Infrared Observations; Mineralogy

1 Introduction

The NASA *Deep Impact* (DI) encounter with Comet 9P/Tempel 1 on July 4, 2005 (A'Hearn et al. 2005) provided a rich and unique collection of data obtained with a range of instruments (Hampton et al. 2005). For example, the InfraRed spectrometer on the High–Resolution Instrument (HRI–IR) produced nucleus spectra in the wavelength range $1.04 \leq \lambda \leq 4.89\,\mu$m with a resolving power $200 \leq \lambda/\Delta\lambda \leq 800$. In 2×2 binning mode a data matrix is obtained with 512 wavelength bins for 256 spatial pixels. By exploiting spacecraft rotation and performing repeated imaging, 40×256 pixel scans could be produced, where each pixel represents a full spectrum. A single scan obtained during the flyby (#9000036) contains the entire visible side of the nucleus (resolved by ~ 1000 pixels) obtained 15800 km from the comet, ~ 26 min prior to closest approach. This scan was used by Groussin et al. (2007) to produce the first 2D surface temperature map of a comet nucleus. By applying a thermophysical model to produce synthetic temperature maps and comparing these with the empirical data, Groussin et al. (2007) also concluded that the thermal inertia $\mathcal{I}$ of the nucleus must be very low, preferably $\mathcal{I} \leq 50\,\mathrm{J\,m^{-2}\,K^{-1}\,s^{-1/2}}$.

The analysis by Groussin et al. (2007) is an impressive and important first step towards a deeper understanding of the surface conditions of comets. However, certain assumptions have been made that potentially may bias the results and interpretations in a certain direction. For example, small scale surface roughness (i.e., nucleus topography on subpixel scales) has not been taken into account. Small scale surface roughness affects the properties of thermal emission spectra (hence the procedure used to estimate surface temperatures), as well as the thermophysical model needed to interpret those temperatures (inclusion of self heating). It can therefore not be excluded that conclusions regarding, e.g., the thermal inertia of the nucleus may have to be revised if small scale surface roughness is taken into consideration.

Here, an independent analysis of the scan #9000036 spectra is performed, using an approach suitable for a body with surface roughness. The methods, theories and models necessary for this work are summarized in Sec. 2 (certain related equation derivations and error investigations are given in Appendices A–D). Specifically, Sec. 2.1 deals with the extraction of spectral reddening,

surface temperature, and the product of the beaming function and directional emissivity[1] from the spectra. Section 2.2 describes the nucleus geometrical model, the thermophysical model, the division of the surface into morphological surface units, as well as the method used to estimate the small scale self heating parameter and the thermal inertia of the nucleus. Section 2.3 summarizes a surface roughness model based on considering circular paraboloid pits, which is used to provide possible interpretations of the small scale self heating parameter. Combined with Hapke theory the model is also used to produce a theoretical beaming function. In Sec. 2.4, a method used to estimate the volume emissivity factor of the nucleus surface material is described. Furthermore, we explain how Mie theory here is used to place constraints on grain size and composition. Finally, the results are presented in Sec. 3 and discussed in Sec. 4.

Table 1 summarizes all parameter symbols used throughout this paper.

Table 1.

2 Methods, Theories, and Models

2.1 Interpreting the HRI–IR Spectra

The spectra composing scan #9000036 with accompanying spectral registration are available in the NASA Planetary Data System (PDS) archive[2]. These spectra have already been reduced with the DI pipeline, thus providing intensity as function of wavelength, $I_{\mathrm{DI}}(\lambda)$ [$\mathrm{J\,m^{-2}\,s^{-1}\,ster^{-1}\,\mu m^{-1}}$]. However, intensity spikes caused by bad pixels intentionally remained, hence a simple method to identify and remove such spikes was employed. A typical spectrum after bad pixel removal is seen in the upper left panel of Fig. 1. A pixel was considered on–nucleus if the mean intensity in the $3.0 \leq \lambda \leq 3.6\,\mu$m region exceeded $0.07\,\mathrm{J\,m^{-2}\,s^{-1}\ ster^{-1}\,\mu m^{-1}}$. The mean intensity cut–off value is arbitrarily chosen, but is two orders of magnitude smaller than the nucleus peak value and one order of magnitude larger than the background average. A $\lambda \leq 3.6\,\mu$m cut–off is used throughout this work due to the existence of anomalous intensity discontinuities (vertical displacement of parts of the spectrum) seen for several pixels at larger wavelengths.

Fig. 1.

[1] In this paper we distinguish between directional, hemispherical, and integrated emissivities, see Hapke (1993).
[2] http://pds.jpl.nasa.gov/

The spectrum of the solar light scattered off the nucleus $I_R(\lambda)$ is modeled by using a solar spectrum from the PDS archive[3], reddened by R and normalized to coincide with $I_{\rm DI}$ at $1.69 \leq \lambda \leq 1.71\,\mu$m. Here, $0 \leq R \leq 10\,\%\,{\rm k\AA}^{-1}$ is considered with $0.1\,\%\,{\rm k\AA}^{-1}$ resolution. For each R–value a chi–square proxy,

$$\chi^2_R = \sum_\lambda \left(I_{\rm DI} - I_R\right)^2 \tag{1}$$

is calculated for the $1.2 \leq \lambda \leq 2.5\,\mu$m region and the R–value corresponding to the smallest χ^2_R is selected as the reddening for the pixel in question. Given the 10% uncertainty in the absolute calibration of $I_{\rm DI}$ (Groussin et al. 2007), the 1–σ error in fitted reddening amounts to $\pm 0.06\,\%\,{\rm k\AA}^{-1}$ on average for the considered pixels. Our $\pm 0.05\,\%\,{\rm k\AA}^{-1}$ error bars due to the fitting procedure therefore roughly correspond to 1–σ. Such a fit is exemplified in the upper right panel of Fig. 1. It is noted that Groussin et al. (2007) assumed $R = 3.0\%\,{\rm k\AA}^{-1}$ for all spectra.

Subtracting the best fit $I_{\rm R}(\lambda)$ from $I_{\rm DI}(\lambda)$ yields the thermal emission spectrum $I_{\rm th}(\lambda)$, exemplified in the lower left panel of Fig. 1. The thermal spectrum is modeled by a function

$$I_\lambda = \frac{\Lambda \varepsilon_{\rm d}}{\pi} B_\lambda(T) \tag{2}$$

where the Planck function $B_\lambda(T)$ depends on wavelength and temperature T according to

$$B_\lambda(T) = \frac{2\pi h c^2}{\lambda^5} \left(\exp\left(\frac{hc}{k\lambda T}\right) - 1\right)^{-1} \tag{3}$$

where h is the Planck constant, c is the speed of light in vacuum, and k is the Boltzmann constant. The directional emissivity $\varepsilon_{\rm d}$ is a function of wavelength, viewing geometry, and surface material properties (e.g., composition and particle size), accounting for the fact that a macroscopically flat surface[4] of a particulate medium does not emit radiation like a black body. The total emitted power is reduced with respect to a black body at the same temperature in case light scattering occurs (e.g., at optical wavelengths) and the solid angle intensity distribution may not be isotropic (as is the case for black body radiation) due to radiative transfer processes in the particulate medium. The beaming function Λ is a function of wavelength, viewing geometry, surface material properties

[3] hriir_020601_2_0.tab

[4] By "macroscopic" we mean size scales much larger than the typical grain size of the medium.

and surface topography, accounting for the fact that a macroscopically rough surface does not emit radiation in the same way as a macroscopically flat surface since there is a variety of local surface normals across the surface.

It is assumed that $\varepsilon_{\rm d}$ and Λ do not depend strongly on wavelength in the interval $3.0 \leq \lambda \leq 3.6\,\mu$m (*no* constraints are placed on the wavelength dependence outside this range). Denoting their product by $X' = \Lambda\varepsilon_{\rm d}$, the model function therefore has two free parameters $\{X', T\}$ in addition to the wavelength dependence,

$$I_\lambda(X', T) = \frac{X'}{\pi} B_\lambda(T), \tag{4}$$

which are evaluated for each pixel as follows.

A grid of $I_\lambda(X', T)$ models is calculated for $0.05 \leq X' \leq 1$ with 0.05 resolution and $200 \leq T \leq 350\,$K with 0.5 K resolution. For each $\{X', T\}$ combination a chi–square proxy of I_λ with respect to the empirical spectrum $I_{\rm th}$ is calculated for the $3.0 \leq \lambda \leq 3.6\,\mu$m region,

$$\chi^2_{\rm th} = \sum_\lambda \Big(I_{\rm th}(\lambda) - I_\lambda(X', T) \Big)^2, \tag{5}$$

and the combination $\{X', T\}$ yielding the smallest $\chi^2_{\rm th}$ is taken as the solution for the pixel in question. An example of such a solution is seen in the lower right panel of Fig. 1. It is noted that Groussin et al. (2007) in practice assumed $X' = 0.9$ for all spectra.

Since only a small part of the short–wavelength wing of the emission Wien peak is available for analysis it is important to verify that physically meaningful pairs X' and T indeed can be extracted – this is done in Appendix A.

2.2 Thermophysics

In order to interpret the temperature map obtained from the HRI–IR spectra it is necessary to use a thermophysical model. Such models require knowledge of local illumination conditions on the nucleus surface, hence it is mandatory to first define a geometrical shape model of the nucleus. We apply the shape model available in the PDS archive (Thomas et al. 2007), consisting of 3D Cartesian position coordinates for 16471 surface node points, which may be used to divide the

surface into 32400 triangular facets. Given the nucleus orientation with respect to the spacecraft at the time of scan #9000036, 17225 of these facets are in the field of view while the rest are on the nucleus far side. On average, visible facets have an area of $3.5 \cdot 10^3\,\mathrm{m}^2$, corresponding to an equal–area circle of radius 33 m. Henceforth, the phrase "global topography" applies to shape features resolved by this geometrical nucleus model, while the phrase "small scale roughness" (or just "roughness") refers to unresolved topography. Each facet is considered to have a flat shape on average (i.e., its surface normal is representative for the terrain in question), but may have irregularities on size scales $\lesssim 10\,\mathrm{m}$.

Each model facet may be considered a member of a certain HRI–IR pixel in scan #9000036 by having the majority of its surface within the field of view of that pixel – the "mother pixel". The pixel size (projected onto the nucleus) varied from 163 m to 152 m during the scan due to spacecraft motion. On average, there are ~ 7 facets within each pixel.

In the thermophysical model, it is assumed that the modeled surface layer (with a thickness of a few meters) consists of non–volatile material characterized by the thermal inertia $\mathcal{I}$ and the integrated emissivity $\overline{\varepsilon}_\mathrm{h}$. We assume that the dust mantle is thicker than the modeled slab in order to avoid a redefinition of $\mathcal{I}$ at the ice sublimation front. Since Sunshine et al. (2007) showed that the devolatilized layer at the DI impact site on 9P/Tempel 1 was about one meter thick, we consider our assumption reasonable. The surface may have roughness, characterized by the small scale self heating parameter ξ (Lagerros 1997). A spatially one–dimensional governing equation is applied, describing heat conduction along the local average inward surface normal (e.g., for a facet in the geometrical nucleus model),

$$\frac{\partial T}{\partial t} = \frac{\omega}{2} \frac{\partial^2 T}{\partial x_*^2}, \tag{6}$$

where T is temperature, t is time, $\omega = 2\pi/P$ (P is the nucleus rotational period), and x_* is a dimensionless depth parameter (physical depth x over $\sqrt{2}$ times the thermal skin depth). One may translate x_* to a physical depth by assigning a density ρ, specific heat capacity C, and conductivity

κ to the material (e.g., Groussin et al. 2004),

$$x = x_* \sqrt{\frac{2\kappa}{\rho C \omega}} \tag{7}$$

where those quantities must be consistent with the assumed thermal inertia, $\mathcal{I} = \sqrt{\rho C \kappa}$.

The surface boundary condition to Eq. (6) is given by

$$\frac{S_\odot (1-A) \max\{\mu(t),\, 0\}}{r_\mathrm{h}^2} = X \sigma_\mathrm{SB} T^4 - \sqrt{\frac{\omega}{2}} \mathcal{I} \frac{\partial T}{\partial x_*}\Big|_{x_*=0} \tag{8}$$

where $S_\odot$ is the solar constant, A is the bolometric Bond albedo, r_h is the heliocentric distance, $\mu(t)$ is the average cosine of the local solar zenith angle for the rough surface, σ_SB is the Stefan–Boltzmann constant, and the parameter[5] X is given by

$$X = (1 - \overline{\varepsilon}_\mathrm{h} \xi) \overline{\varepsilon}_\mathrm{h}. \tag{9}$$

Equation (8) is derived in Appendix B and includes a suppressed capability of a rough surface to dissipate heat by thermal reradiation into space (compared to a flat surface with the same T), which leads to small scale self heating.

With a solar co–declination d_co (angle between the nucleus positive spin pole and the solar direction) and the co–latitude l_co (angle between the nucleus positive spin pole and the local average outward surface normal), $\mu(t)$ is given by

$$\mu(t) = \cos d_\mathrm{co} \cos l_\mathrm{co} + \sin d_\mathrm{co} \sin l_\mathrm{co} \cos \omega (t - t_0), \tag{10}$$

where $t_0 = 20.35\,\mathrm{h}$ is the time of local solar culmination (the rotational period is $P = 40.7\,\mathrm{h}$ according to Table 2 and $t = 0$ corresponds to local midnight). Table 2.

We emphasize that we make full usage of the Thomas et al. (2007) shape model throughout this paper, e.g., when working with Eq. (10). Specifically, local surface normals are taken as the facet surface normals of the irregular body, i.e., are uncorrelated to the position vectors of facet centers as seen from the shape model origin. Therefore, the co–latitude is uncorrelated to latitudes and longitudes, since it is only depending on the local surface normal orientation with respect to

[5] We avoid the terminology "beaming factor" and symbol "η" normally used in the asteroid Standard Thermal Model (Lebofsky and Spencer 1989) since that model does not include heat conduction (hence $X \neq \eta$).

the spin pole. Local times t are calculated from the local surface normal orientation with respect to the plane containing the Sun and the spin axis. Hence, it is possible that physically close regions have very different local time. Also, quasi–flat regions with a substantial latitudinal and longitudinal extension will have a rather small internal variation in the local time.

Equation (10) is not applicable for facets on the model nucleus that are subjected to global self heating and/or shadowing due to global topography. Hence such facets need to be identified and excluded from the current investigation, which is described in Appendix C.

At a depth x'_* where diurnal temperature fluctuations are negligible, the boundary condition

$$\frac{\partial T}{\partial x_*}\Big|_{x_*=x'_*} = 0 \tag{11}$$

is applied.

The thermophysical model summarized by Eqs. (6)–(11) contains a number of parameters which are considered to be known (Belton et al. 2006; Thomas et al. 2007; Li et al. 2007), according to Table 2. For a given co–latitude $l_{\rm co}$, the model therefore only contains two free physical parameters, X and $\mathcal{I}$. The following procedure is applied in an attempt to constrain X and $\mathcal{I}$ by requiring that the thermophysical model reproduces the temperature map obtained in Sec. 2.1.

First a database of thermophysical models is produced by considering all combinations of co–latitudes $0^\circ \leq l_{\rm co} \leq 168^\circ$ with 2° resolution[6], X–values $0.05 \leq X \leq 1$ with 0.05 resolution, and thermal inertia (in units of $[\mathrm{J\,m^{-2}\,K^{-1}\,s^{-1/2}}]$) of $10 \leq \mathcal{I} \leq 100$ (resolution 10), $\mathcal{I} = 150$, $200 \leq \mathcal{I} \leq 800$ (resolution 100), $1000 \leq \mathcal{I} \leq 3500$ (resolution 500), i.e., 40800 models in total. The thermophysical differential equation is solved using the Finite Element Method, considering $x'_* = 20$, using 100 spatial cells, a time step of 24 s and performing a sufficient number of nucleus revolutions to guarantee that the difference between absorbed and emitted energy fluxes (integrated over one nucleus revolution) is $\leq 1\%$ of the integrated absorbed flux. That is to say, steady–state is reached in the sense that the solution $T(x,t)$ is repeated from one revolution to the next.

[6]There are no illuminated facets with $l_{\rm co} > 168^\circ$.

Typically, 5–20 nucleus revolutions are required to reach steady–state, corresponding to a real time between a week and a month. However, this relaxation time is heavily dependent on the initial temperature profile for each model, which is chosen somewhat arbitrarily. A poor initial guess may result in a long relaxation time, which has nothing to do with the capability of the real nucleus to adjust to changes in illumination conditions throughout the orbit, since these are smooth and gradual. We note that the DI encounter with Comet 9P/Tempel 1 took place one day before perihelion, i.e., the comet was still on the inbound part of its orbit. If the nucleus displays any sign of seasonal thermal lag (in the near–surface layer), we would expect measured temperatures being *lower* than those predicted by a steady–state model (e.g., evaluated for a standard parameter combination of $\{X, \mathit{\Gamma}\} = \{0.9, 10\}$). As it turns out, the measurements indicate temperatures significantly *higher* than those predicted by the aforementioned model. This leads us to believe that seasonal thermal lag is not an issue in this case, i.e., steady–state models can be used for the current study.

To build empirical temperature functions to be compared with model solutions, the nucleus is divided into co–latitude slabs (*not* trivially related to latitudes on a irregular nucleus) of thickness 2°–8° depending on the local sensitivity of temperature on $l_{\rm co}$. Considering one $l_{\rm co}$–slab at a time, all facets on the visible side of the nucleus with their co–latitudes within that slab (except excluded facets, see Appendix C) are identified. These are arranged in order of increasing local hour and are assigned temperatures according to their mother pixels. Thereby, empirical temperature functions $T_{\rm emp} = T_{\rm emp}(t)$ are formed, each valid for a certain co–latitude. Fig. 2

The surface of Comet 9P/Tempel 1 consists of several types of terrain, which led Thomas et al. (2007) to define various morphological units based on their visible appearance. In Fig. 2 we show a cartoon based on Fig. 8B of Thomas et al. (2007), where the boundaries for seven morphological units have been reproduced, here labeled 1–7 for simplicity. Units 1 and 5 constitute so–called thin layers terrain, units 2 and 6 are smooth terrain, units 3 and 7 are scarped/pitted terrain, while unit 4 is thick layers terrain. The $T_{\rm emp}(t)$ functions generally cross several morphological units and it cannot be excluded that the surface roughness and thermal inertia vary from unit

to unit. It is therefore not safe to attempt to fit an entire $T_{\rm emp}(t)$ curve at once. Therefore, the $T_{\rm emp}(t)$ curves are *divided into segments, each corresponding to a single morphological unit.* At this point we also exclude morphological unit 2 from the investigation. The reason is that unit 2 is known to contain surface ice (Sunshine et al. 2006) and Eq. (8) ignores energy consumption due to sublimation. We also disregard $T_{\rm emp}(t)$ segments extending less than 0.5 h in hour angle.

The remaining $T_{\rm emp}(t)$ segments are binned into 0.2 h–wide bins, and the temperature is averaged within each bin. Due to uncertainties in the HRI–IR absolute flux calibration (Groussin et al. 2007) we assign $\Delta T_{\rm emp} = \pm 7\,{\rm K}$ error bars, unless the standard deviation of the temperature for data points within the bin is larger, in which case that value is used.

In order to estimate the likely $\{X, \mathcal{I}\}$ values of the nucleus for a certain morphological unit, at a certain $l_{\rm co}$, we calculate the chi–square χ^2 of all relevant theoretical temperature curves $T = T(X, \mathcal{I}, t)$ (i.e., those with the correct $l_{\rm co}$) with respect to the M data points constituting the $T_{\rm emp}(t)$ curve segment in question,

$$\chi^2(X, \mathcal{I}) = \sum_M \left(\frac{T_{\rm emp}(t) - T(X, \mathcal{I}, t)}{\Delta T_{\rm emp}(t)} \right)^2 . \tag{12}$$

We then take the parameter pair $\{X, \mathcal{I}\}$ with the smallest χ^2 as the most likely solution. The credibility of such "best fit solutions" increases further if several $l_{\rm co}$ slabs from the same morphological unit yield similar solutions. To assign error bars to the best fits we also evaluate the incomplete gamma function for all models,

$$Q(b, w) = \frac{\int_w^\infty e^{-z} z^{b-1}\, dz}{\int_0^\infty e^{-z} z^{b-1}\, dz}, \tag{13}$$

where $b = \nu/2$ and $w = \chi^2(X, \mathcal{I})/2$, where the number of degrees of freedom is $\nu = M - 2$ since we have two independent model parameters X and $\mathcal{I}$ (see, e.g., Press et al. 1986). We form error bars at a confidence level of $1 - Q = 99\%$ (roughly corresponding to 3–σ), by considering all $\{X, \mathcal{I}\}$ models for which[7] $Q \geq 0.01$. However, we also consider the consequences of using the smaller 1–σ error bars corresponding to a confidence level of 68.3%, or a $Q \geq 0.317$ criterion for the models.

[7]Hence, the error margins include solutions with such large χ^2 that there is only 1% probability that the real $\{X, \mathcal{I}\}$ solution will have a chi–square this large or larger, by chance.

This procedure therefore allows us to estimate how X and the thermal inertia $\mathcal{I}$ vary across the nucleus disk. Since $\overline{\varepsilon}_{\rm h}$ is considered known (Table 2), X and Eq. (9) then yields the small scale self heating parameter ξ as a function of surface position.

From the derived thermal inertia it may be interesting to estimate a corresponding porosity ψ of the medium. Since this estimate is strongly model dependent, it should be considered an *example* rather than an attempt to actually determine the porosity.

Here this is done by considering a mixture of the pyroxene enstatite ($MgSiO_3$) and the olivine forsterite (Mg_2SiO_4) as a representative surface material. In compact form, enstatite ($T = 300\,\mathrm{K}$) is characterized by $\rho_{\rm comp} = 3270\,\mathrm{kg\,m^{-3}}$, $C = 830\,\mathrm{J\,kg^{-1}\,K^{-1}}$ and $\kappa_{\rm comp} = 4.47\,\mathrm{J\,m^{-1}\,s^{-1}\,K^{-1}}$, yielding a thermal inertia of $\mathcal{I}_{\rm comp} = 3480\,\mathrm{J\,m^{-2}\,K^{-1}\,s^{-1/2}}$. Compact forsterite ($T = 300\,\mathrm{K}$) is characterized by $\rho_{\rm comp} = 3280\,\mathrm{kg\,m^{-3}}$, $C = 840\,\mathrm{J\,kg^{-1}\,K^{-1}}$ and $\kappa_{\rm comp} = 5.12\,\mathrm{J\,m^{-1}\,s^{-1}\,K^{-1}}$, yielding a thermal inertia of $\mathcal{I}_{\rm comp} = 3760\,\mathrm{J\,m^{-2}\,K^{-1}\,s^{-1/2}}$. Here, densities and heat conductivities are taken from Horai (1971), while the specific heat capacities are taken from Richet et al. (1993) and Robie et al. (1982).

To estimate the conductivity of a porous medium $\kappa = \kappa_{\rm comp}\Phi(\psi)$, we apply the hierarchical fractal "generation three" model of Shoshany *et al.* (2002) with percolation threshold $p_{\rm c} = 0.7$,

$$\begin{cases} \Phi(\psi) = \left(1 - \dfrac{p(\psi)}{p_{\rm c}}\right)^{12.3p(\psi)+0.66} \\ \\ p(\psi) = 1 - (1-\psi)^{\frac{1}{3}}\,. \end{cases} \tag{14}$$

Since the heat capacity ρC decreases linearly with increasing porosity, we may obtain a possible porosity of the surface material from the estimated thermal inertia $\mathcal{I}$ by solving the following expression for ψ,

$$\begin{aligned} \mathcal{I} &= \sqrt{\rho_{\rm comp} C (1-\psi) \kappa_{\rm comp} \Phi(\psi)} \\ &= \mathcal{I}_{\rm comp}\sqrt{(1-\psi)\Phi(\psi)}, \end{aligned} \tag{15}$$

where we assume $\mathcal{I}_{\rm comp} = 3620\,\mathrm{J\,m^{-2}\,K^{-1}\,s^{-1/2}}$, i.e. the mean value for enstatite and forsterite.

2.3 The Surface Roughness Model

For illustrative purposes we define here a simple model of surface roughness in order to interpret the estimated small scale self heating parameter ξ, as well as calculating a beaming function Λ to be used when analyzing the X' map discussed in Sec. 2.1. It will be assumed that an area fraction f of an otherwise flat terrain consists of pits. If the integrated surface area of a pit is $A_{\rm pit}$ and if the rim encircles a flat area $A_{\rm rim}$, the total integrated area of the rough terrain is given by $A_{\rm rough} = (1-f)A_{\rm flat} + f\frac{A_{\rm pit}}{A_{\rm rim}}A_{\rm flat}$, where $A_{\rm flat}$ is the projected flat surface area of the terrain in question. By definition (Lagerros 1997), we have

$$\begin{aligned} \xi &= 1 - \frac{A_{\rm flat}}{A_{\rm rough}} \\ &= 1 - \frac{A_{\rm rim}}{(1-f)A_{\rm rim} + fA_{\rm pit}}. \end{aligned} \tag{16}$$

Here, the pits are modeled as circular paraboloids parameterized by their depth–to–diameter ratio S. We choose this model since it is not limited to $S \leq 0.5$ as is the case for spherical pits used by many authors (e.g., Hansen 1977; Lagerros 1997). For such a model,

$$A_{\rm rim} = 64\pi S^2, \tag{17}$$

$$A_{\rm pit} = \frac{8}{3}\pi\left((16S^2+1)^{3/2} - 1\right). \tag{18}$$

Furthermore, if d is the depth of the pit measured in units of the distance between the paraboloid focus and vertex at the pit bottom, then $d = 16S^2$. Inserting Eqs. (17) and (18) into Eq. (16) yields ξ as function of f and S for the model,

$$\xi(S,f) = 1 - \left(1 - f + \frac{f}{24S^2}\left\{\left(16S^2+1\right)^{3/2} - 1\right\}\right)^{-1}. \tag{19}$$

Given a certain ξ estimate obtained as described in Sec. 2.2 one may therefore consider a relation $f = f(S)$ that must be fulfilled,

$$f(S) = \frac{\xi}{1-\xi}\left(\frac{1}{24S^2}\left\{\left(16S^2+1\right)^{3/2} - 1\right\} - 1\right)^{-1}. \tag{20}$$

A beaming function $\Lambda(S,\, f,\, \mu_{\rm e},\, \gamma)$ consistent with the circular paraboloid pit model can be calculated numerically as function of S, f, the cosine of the emission angle $\mu_{\rm e}$, and the volume

emissivity factor γ^2 (see Sec. 2.4) of the surface grains. This procedure is described in some detail in Appendix D.

By using the modeled beaming function and the Hapke (1993) expression for directional emissivity,

$$\varepsilon_{\rm d}(\mu_{\rm e},\,\gamma) = \gamma\frac{1+2\mu_{\rm e}}{1+2\gamma\mu_{\rm e}}, \tag{21}$$

a model equivalent to the X' parameter (see, Sec. 2.1, particularly Eq. (4)) is obtained,

$$X'_{\rm mod}(S,\,f,\,\mu_{\rm e},\,\gamma) = \Lambda(S,\,f,\,\mu_{\rm e},\,\gamma)\varepsilon_{\rm d}(\mu_{\rm e},\,\gamma). \tag{22}$$

The variation of $\mu_{\rm e}$ across the nucleus disk is obtained from the geometrical nucleus model, and Eq. (20) yields a relation between S and f, which reduces the number of free parameters to two, $X'_{\rm mod} = X'_{\rm mod}(S,\,\gamma)$. Fortunately, the S–dependence turns out to be very weak. Therefore, for any given facet on the nucleus $X'_{\rm mod}$ is primarily a function of the volume emissivity factor γ^2. By matching $X'_{\rm mod}$ with X' obtained directly from the HRI–IR spectra, one can therefore estimate how γ^2 varies across the nucleus disk – although this estimate of course relies on the assumption that the applied surface roughness model is reasonable. It is emphasized that the estimated γ^2 is valid for the wavelength range $3.0\,\mu{\rm m} \leq \lambda \leq 3.6\,\mu{\rm m}$, since this is where X' has been fitted.

2.4 Mie Modeling

The volume emissivity factor γ^2 is defined as the ratio between the absorption coefficient $Q_{\rm A}$ and the extinction coefficient $Q_{\rm E}$ of the constituent particles,

$$\gamma^2 = \frac{Q_{\rm A}}{Q_{\rm E}}. \tag{23}$$

Assuming that the grains are spherical, both $Q_{\rm A}$ and $Q_{\rm E}$ can be calculated as functions of wavelength, grain size and composition by using Mie theory (e.g., Bohren and Huffman 1983). We use the code DMILAY written by Toon and Ackerman (1981) to produce modeled volume emissivity factors $\gamma^2_{\rm mod}$. Here, we consider a range of grain sizes $0.01\,\mu{\rm m} \leq a \leq 100\,\mu{\rm m}$ and use wavelength–dependent complex refractive indices of seven representative species likely to be encountered on a cometary surface; pyroxene $\rm Mg_{1-\mathit{y}}Fe_{\mathit{y}}SiO_3$ with $y = \{0.0,\,0.2,\,0.4,\,0.6\}$ (Dorschner

et al. 1995); $Fo_{50}Fa_{50}$ olivine $MgFeSiO_4$ (Dorschner et al. 1995); troilite FeS (Pollack et al. 1994); carbon C (Jäger et al. 1998).

In order to constrain the grain size of the surface material, the hemispherical emissivity is first calculated (Hapke 1993) for each grain size and substance,

$$\varepsilon_{\mathrm{h,mod}}(\lambda) = \frac{2\gamma_{\mathrm{mod}}}{1+\gamma_{\mathrm{mod}}}\left(1+\frac{1}{6}\frac{1-\gamma_{\mathrm{mod}}}{1+\gamma_{\mathrm{mod}}}\right) \tag{24}$$

remembering that $\gamma_{\mathrm{mod}} = \gamma_{\mathrm{mod}}(\lambda)$. The integrated emissivity is then by definition,

$$\overline{\varepsilon}_{\mathrm{h,mod}} = \frac{1}{\sigma_{\mathrm{SB}}T^4}\int_0^\infty \varepsilon_{\mathrm{h,mod}}(\lambda)B_\lambda(T)\,d\lambda. \tag{25}$$

Calculating $\overline{\varepsilon}_{\mathrm{h,mod}}$ for a range of relevant temperatures, substances, and grain sizes, and comparing it to the empirical value $\overline{\varepsilon}_{\mathrm{h}}$ in Table 2 places plausible constraints on the grain size of the medium. Focusing on the constrained grain size range and the wavelength region $3.0\,\mu\mathrm{m} \le \lambda \le 3.6\,\mu\mathrm{m}$ (for which the γ^2 map derived in Sec. 2.3 is valid), a comparison between γ^2_{mod} and γ^2 enables us to discuss constraints on the mineralogical composition of the surface material.

3 Results

3.1 Reddening, X', and Temperature

We here present the results obtained regarding spectral reddening (at $1.2 \le \lambda \le 2.5\,\mu\mathrm{m}$), the product between beaming function and directional emissivity X' (at $3.0\,\mu\mathrm{m} \le \lambda \le 3.6\,\mu\mathrm{m}$) as well as the nucleus surface temperature, using the approach described in Sec. 2.1.

The estimated median reddening of the nucleus is $\langle R\rangle_{\mathrm{med}} = 3.5\,\%\,\mathrm{k\AA}^{-1}$ and $\sim 92\%$ of the pixels have $2.5\,\%\,\mathrm{k\AA}^{-1} \le R \le 4.5\,\%\,\mathrm{k\AA}^{-1}$. A few pixels ($\sim 4\%$) have comparatively high reddening ($R \ge 6.0\,\%\,\mathrm{k\AA}^{-1}$), all lining up along the eastern limb (to the right in Fig. 2). A similar limb discontinuity in color is seen in Fig. 10 (right panel) in the paper by Li et al. (2007), and is there attributed to mis–registration and/or differences in the point spread function at different wavelengths. Groussin et al. (2007) also point out that light scattering problems within the HRI–IR instrument are present, being strongest in areas with rapid changes in contrast, i.e., at the limb

and for large shadowed regions on the nucleus. Therefore, we consider pixels with $R \geq 6.0\,\%\,\mathrm{k\AA}^{-1}$ unphysical and exclude them. Fig. 3

The spectral reddening map for pixels with $2.5\,\%\,\mathrm{k\AA}^{-1} \leq R \leq 4.5\,\%\,\mathrm{k\AA}^{-1}$ is seen in the upper left panel of Fig. 3, remembering the $\pm 0.05\,\%\,\mathrm{k\AA}^{-1}$ (roughly 1–σ) error bars[8]. The variation in R across the nucleus disk is large enough to be statistically significant and the resulting pattern is clearly not random (there are large coherent areas with similar R). The structures are at least partially related to the location of morphological units. In particular unit 6 (smooth terrain) and unit 4 (thick layers terrain), are distinguishable by being visibly different from their immediate surroundings (they are slightly redder than average, both having $\langle R \rangle_{\mathrm{med}} = 3.6\,\%\,\mathrm{k\AA}^{-1}$). Unit 5 contains two areas with different degrees of reddening, which seem to correlate with layers c and d defined by Belton *et al.* (2007) in their Fig. 2. The only identified region containing surface water ice (Sunshine et al. 2006), i.e. unit 2 (smooth terrain), stands out by having the smallest degree of spectral reddening of any unit, $\langle R \rangle_{\mathrm{med}} = 3.2\,\%\,\mathrm{k\AA}^{-1}$.

The map of $X' = \Lambda\varepsilon_{\mathrm{d}}$ seen in the upper right panel of Fig. 3 shows a strong correlation with the location of morphological units. For unit 3 and the southern part ($l_{\mathrm{co}} \gtrsim 125°$) of unit 7 (both scarped/pitted terrains), X' is noticeably smaller than unity with a median $\langle X' \rangle_{\mathrm{med}} = 0.75$ and mean $\langle X' \rangle_{\mathrm{mean}} = 0.67$. The other regions on the nucleus are characterized by $\langle X' \rangle_{\mathrm{med}} = 1$. Particularly the boundary between units 3 and 4 coincide with a noticeable change in X'. This clearly shows that the HRI–IR spectra not only depend on temperature, but also on factors like material properties (e.g., composition and grain size), surface roughness and viewing geometry, that apparently vary measurably between morphological units. The fact that patterns of morphological units are clearly visible in the upper panels of Fig. 3 also confirms that the techniques used to extract R and $\{X', T\}$ generally are reliable.

The lower left panel of Fig. 3 shows the surface temperature, which varies between $271 \leq T \leq 331\,\mathrm{K}$ ($\pm 7\,\mathrm{K}$). The temperatures we obtain are very similar to those obtained by Groussin

[8]The reason for excluding a few pixels with $R < 2.5\,\%\,\mathrm{k\AA}^{-1}$ or $R > 4.5\,\%\,\mathrm{k\AA}^{-1}$ in the plot is just to increase the color contrast.

et al. (2007) despite the difference in how X' is treated in the two investigations. A test where $R = 3.0\,\%\,\mathrm{k\mathring{A}}^{-1}$ and $X' = 0.9$ are enforced, shows that the median and mean differences in temperature between the two approaches are $\langle|\Delta T|\rangle_{\rm med} = 1.5\,\mathrm{K}$ and $\langle|\Delta T|\rangle_{\rm mean} = 5.0\,\mathrm{K}$, respectively. Furthermore, the difference is less than 7 K for 76% of the pixels. Therefore, for a majority of the pixels, differences in temperature are within the assigned error bars.

3.2 Surface Roughness and Thermal Inertia

We here summarize the results obtained by applying the procedures in Sec. 2.2 in order to estimate the small scale self heating parameter ξ and the thermal inertia $\mathcal{I}$ by thermophysical model reproduction of the temperature map seen in the lower left panel of Fig. 3. Fig. 4

To exemplify the analysis, the upper panel of Fig. 4 shows the empirical nucleus temperature $T_{\rm emp}(t)$ at co–latitude $l_{\rm co} = 38^\circ \pm 2^\circ$ for morphological unit 3 (circles with error bars). The lower panel shows models in $\{X, \mathcal{I}\}$ space which fulfill the $Q \geq 0.01$ criterion, i.e., yield theoretical curves $T(t)$ that are statistically consistent with $T_{\rm emp}(t)$ and its error bars at 99% confidence level. In this case, solutions with $0.30 \leq X \leq 0.65$ are possible, which translates to a small scale surface roughness $0.35 \leq \xi \leq 0.71$ if applying Eq. (9) and Table 2.

Evidently, a significant degree of surface roughness is necessary to reproduce the nucleus surface temperature. For the smallest allowed degree of roughness (largest X), the model predicts a thermal inertia that may be as low as $\mathcal{I} = 10\,\mathrm{J\,m^{-2}\,K^{-1}\,s^{-1/2}}$. However, in case the surface is rougher, a larger thermal inertia is needed to reproduce the temperature curve, including values as high as $\mathcal{I} = 3500\,\mathrm{J\,m^{-2}\,K^{-1}\,s^{-1/2}}$.

To illustrate the variety of accepted solutions, the upper panel of Fig. 4 shows two examples (a third dotted curve is discussed in Sec. 4.1.3). The dashed–dotted curve shows $T(t)$ for a $\{X, \mathcal{I}\} = \{0.65, 10\}$ model, to illustrate the behavior of an accepted model with very low thermal inertia. The fit may not be entirely convincing if solely relying on the visual impression, since the morning temperatures are too low and the noon temperature tends to be too high. Nevertheless, at 99% confidence level it is not statistically justified to exclude this model. However, applying

1–σ error bars, i.e., a confidence level of 68.3% and a criterion $Q \geq 0.317$, would eliminate this solution and only models with $X = 0.3$ and $\mathcal{I} \geq 800\,\mathrm{J\,m^{-2}\,K^{-1}\,s^{-1/2}}$ would remain.

The particular model yielding the smallest chi–square with respect to $T_{\mathrm{emp}}(t)$ has $\{X, \mathcal{I}\} = \{0.3, 1500\}$, shown as a solid curve in Fig. 4. This model is within the error bars at all considered hour angles and generally reproduces the nominal temperature data points closely. For this model $Q = 1$, and actually 66% of the best fits to the other considered $T_{\mathrm{emp}}(t)$ segments (72 out of 109) have $Q \geq 0.9$. Obtaining such convincing fits may demonstrate that our thermophysical model indeed is suitable for the analysis. However, a Q–value close to unity often only means that the error bars in a measurement simply have been exaggerated. The $\pm 7\,\mathrm{K}$ uncertainty used here is indeed large (compared to changes in T_{emp} with time), but it must be remembered that these error bars are not dominated by random uncertainties, but systematic uncertainties related to calibration. In case the current HRI–IR absolute flux calibration actually *is* accurate, the T_{emp} error bars would shrink to about $\pm 3\,\mathrm{K}$ (truly random errors) and the only surviving solution would be $X \approx 0.3$ and $\mathcal{I} \approx 1500\,\mathrm{J\,m^{-2}\,K^{-1}\,s^{-1/2}}$, i.e., the $\min(\chi^2)$ solution. Hence, we consider the $\min(\chi^2)$ cases the most likely solutions, given the *current* instrument calibration. The $Q \geq 0.01$ error bars shown in the following therefore primarily illustrate the range of possible solutions, should the current calibration change.

To investigate the stability of the best fit solution to changes in the co–latitude slab thickness we also considered cases with $\pm 4°$, $\pm 10°$, and $\pm 20°$, all centered on $l_{\mathrm{co}} = 38°$. It turned out that $\{X, \mathcal{I}\} = \{0.3, 1500\}$ provided the statistically best fit in all cases except when $l_{\mathrm{co}} = 38° \pm 10°$, for which $\{X, \mathcal{I}\} = \{0.3, 2000\}$ had the lowest chi–square. While as the $\pm 2°$ curve used 90 facets from 14 mother pixels to build T_{emp}, the $\pm 4°$ case used 149 facets from 14 mother pixels, the $\pm 10°$ case used 385 facets from 28 mother pixels, and $\pm 20°$ used 523 facets from 41 mother pixels. The number of T_{emp} time bins increased from 28 to 34 with increasing slab thickness. The jump in the number of considered mother pixels when going from $\pm 4°$ to $\pm 10°$ is intimately related to the fact that the variation in facet co–latitudes *within* a certain mother pixel here typically is $\pm 5°$. Therefore, an increase from $\pm 2°$ to $\pm 4°$ primarily incorporates more facets from the same

mother pixels, while the $\pm 10^\circ$ slab extends the sampling to entirely new mother pixels. Since all facets within a certain mother pixel by necessity are assigned the same empirical temperature, the $\pm 5^\circ$ dispersion in surface normals within the mother pixel means that its temperature is smeared out in a ± 0.5 h segment of the $T_{\rm emp}$ curve (roughly corresponding to ± 3 time bins). However, since any given time bin receives temperature contributions that both are lower and higher than the actual temperature, the applied averaging within each bin tends to cancel such uncertainties. Hence, smearing effects should not be severe.

To minimize any possible biasing arising from the aforementioned smearing, we made a test by building a $T_{\rm emp}(t)$ curve for $l_{\rm co} = 38^\circ \pm 2^\circ$, only considering the facet with the largest local hour from within each of the 14 mother pixels. The rationale is that this particular facet has been heated the longest time, it should have the highest temperature among the facets within the mother pixel, and therefore being primarily responsible for the empirical temperature of the mother pixel (by producing an disproportionally large fraction of the observed radiation flux). By avoiding the accidental placement of high temperature data points at small t, we minimize the risk that early morning temperatures are exaggerated, and that the high thermal inertia of the best fit model is an artifact. However, even for this $T_{\rm emp}$ curve, χ^2–minimization occurred for the $\{X, \mathcal{I}\} = \{0.3, 1500\}$ model. Therefore, we do not expect our best fit solutions to be strongly affected by mismatches in resolution between the more detailed shape model and the coarser temperature map from HRI–IR data. The insensitivity of the best fit solutions to changes in slab thickness further illustrates that such problems are small. Fig. 5

We now consider the solutions obtained for X versus co–latitude $l_{\rm co}$, starting with units 1 and 3. These are seen in Fig. 5, e.g., the lower panel includes the previously discussed case at $l_{\rm co} = 38^\circ$ for unit 3 with the $Q \geq 0.01$ error bar, and the $\min(\chi^2)$ solution marked with a circle. Unit 1 (thin layers terrain) has the most likely X–values clustering around $\langle X \rangle = 0.35 \pm 0.04$ (mean $\pm$ standard deviation), which corresponds to $\xi \approx 0.65$. The full range of possible solutions is $0.27 \lesssim \xi \lesssim 0.74$. For unit 3 (scarped/pitted terrain), the most likely solutions have an average $\langle X \rangle = 0.28 \pm 0.07$ ($\xi \approx 0.73$) although there is a trend of higher than average X–values for $l_{\rm co} \lesssim 120^\circ$ (smoother

surface), and lower than average values for $l_{\rm co} \gtrsim 120^\circ$ (rougher surface). That is to say, the southmost region of unit 3 may be very rough ($0.7 \lesssim \xi \lesssim 0.9$), while the tightly constrained X in the $l_{\rm co} = 90^\circ \pm 30^\circ$ region corresponds to $0.55 \lesssim \xi \lesssim 0.7$. Fig. 6

The situation becomes more complicated when considering units 4 (thick layers terrain) and 5 (thin layers terrain), as shown in Fig. 6. The $Q \geq 0.01$ (3–σ) error bars are very large and the most likely solutions jump irregularly between the extreme ends of the error bars. Note that a $Q \geq 0.317$ criterion (1–σ error bars) does not improve the situation, but indicates the existence of a χ^2 double minimum in $\{X, \mathcal{I}\}$ phase space for these units – one at rather high X–values, and another for rather low X–values. To distinguish between the two extremes, the $\min(\chi^2)$ solutions with $X \geq 0.4$ are marked with circles, while $\min(\chi^2)$ solutions with $X < 0.4$ are marked with squares in Fig. 6.

This behavior may be understood by considering Fig. 7. Units 1 and 3 cover the morning and forenoon part of $T_{\rm emp}$ (say $13\,{\rm h} \lesssim t \lesssim 20\,{\rm h}$), where the temperature is sensitive to both X and $\mathcal{I}$. As seen from the $\{X, \mathcal{I}\} = \{0.35, 3500\}$ and $\{0.8, 3500\}$ curves for that t interval in Fig. 7, the *absolute value* of $T(t)$ depends on X, while the $\{X, \mathcal{I}\} = \{0.8, 40\}$ and $\{0.8, 3500\}$ curves show that the *slope* of $T(t)$ is determined by $\mathcal{I}$. Solutions for units 1 and 3 are therefore relatively well constrained. However, units 4 and 5 cover the midday segment of $T_{\rm emp}(t)$ where the temperature changes little with time, and the hour angle coverage is often rather small due to the physically small size of the units. As seen from Fig. 7 at $t \approx 20\,{\rm h}$, the models $\{X, \mathcal{I}\} = \{0.8, 40\}$ and $\{0.35, 3500\}$ are virtually identical, i.e., *a smooth terrain with low thermal inertia is indistinguishable from a rough terrain with high thermal inertia near solar culmination.* The $\min(\chi^2)$ solution could point in either direction by chance, which could explain the behavior in Fig. 6. Fig. 7

In an attempt to decide whether it is more likely that units 4 and 5 are smooth with low thermal inertia, or rough with high thermal inertia, we examine the $\min(\chi^2)$ X–values as a function of the maximum local hour difference of the data sets, with respect to the time of local solar culmination t_0. The idea is, that the farther the data set extends from the $T_{\rm emp}(t)$ peak, the more reliable

is the min(χ^2) solution. Thus, let $\mathcal{H}$ be the range of local hours covered by a particular $T_{\rm emp}(t)$ segment (at a particular $l_{\rm co}$) corresponding to unit 4 or 5. Then $H = \max(|\mathcal{H} - t_0|)$ is the time off–set from local noon of the data point farthest from local solar culmination point. Figure 8 shows X versus H for unit 4 (upper panel) and 5 (lower panel). Fig. 8

As can be seen for unit 4, X is exclusively smaller than ~ 0.4 for large values of H, while ambiguities appear at $H \lesssim 2.7\,$h. Our best guess is therefore that unit 4 is similar to units 1 and 3 in the sense of having substantial surface roughness. Consequently, when trying to define the most likely overall solution for the unit we only consider the min (χ^2) cases in the upper panel of Fig. 6 marked with squares, having $\langle X \rangle = 0.26 \pm 0.11$, which corresponds to $\xi \approx 0.75$. For unit 5, X is exclusively larger than ~ 0.7 for large values of H, while ambiguities appear at $H \lesssim 1.7\,$h. Our best guess is therefore that unit 5 is fundamentally different from units 1, 3, and 4, in the sense of being much smoother. Consequently, we only consider the min (χ^2) solutions in the lower panel of Fig. 6 marked with circles, having $\langle X \rangle = 0.76 \pm 0.14$, which corresponds to $\xi \approx 0.23$.

Of course it cannot be excluded that each min(χ^2) solution actually is real, and that units 4 and 5 indeed have large internal variations in roughness, with a complicated co–latitude dependence. Especially, this may be the case for unit 5, which evidently has internal variations in reddening according to the upper left panel of Fig. 3.

For unit 6, very few data points are available to build the $T_{\rm emp}(t)$ curve since most pixels are removed due to shadowing and self heating problems (the unit is primarily located within a valley on the nucleus). The remaining data points (located at $l_{\rm co} \geq 138^\circ$) yield an average $\langle X \rangle = 0.39 \pm 0.17$, corresponding to $\xi \approx 0.61$. Unit 7 appear to contain two rather different areas. The northern ($l_{\rm co} \lesssim 125^\circ$) part has $\langle X \rangle = 0.67 \pm 0.10$, corresponding to $\xi \approx 0.33$, is comparably smooth and appear similar to the neighboring unit 5 (if accepting the previous guess regarding X). However, the southern ($l_{\rm co} \gtrsim 125^\circ$) part has $\langle X \rangle = 0.26 \pm 0.08$, corresponding to $\xi \approx 0.75$. It is therefore as rough as the southern regions of unit 3. Fig. 9

We now consider the thermal inertia estimated from our modeling. The upper panel of Fig. 9 shows the thermal inertia estimated for unit 1. If only the most likely solutions are considered, we

obtain $\langle \mathcal{I} \rangle = 2500 \pm 1000\,\mathrm{J\,m^{-2}\,K^{-1}\,s^{-1/2}}$ as our best guess, given the current HRI–IR flux calibration. The fact that the independent analysis of temperature curves at ten different co–latitudes consistently yields $\mathcal{I} \geq 1000\,\mathrm{J\,m^{-2}\,K^{-1}\,s^{-1/2}}$ may strengthen the likelihood of this estimate. However, the $Q \geq 0.01$ error bars are generally too large to offer any constraint on $\mathcal{I}$, except for two co–latitudes where a thermal inertia below 300–400 $\mathrm{J\,m^{-2}\,K^{-1}\,s^{-1/2}}$ can be excluded. Reduction of the error bars to 1–σ does not change the situation dramatically, but yield lower limits of 300–400 $\mathrm{J\,m^{-2}\,K^{-1}\,s^{-1/2}}$ at three additional co–latitudes as well as one $\mathcal{I} \geq 1500\,\mathrm{J\,m^{-2}\,K^{-1}\,s^{-1/2}}$ case.

The lower panel of Fig. 9 shows the thermal inertia estimated for unit 3. In this case, the average most likely thermal inertia is $\langle \mathcal{I} \rangle = 1900 \pm 1300\,\mathrm{J\,m^{-2}\,K^{-1}\,s^{-1/2}}$, with a tendency for lower than average values at $l_{\mathrm{co}} \lesssim 70^{\circ}$ and higher than average values at larger co–latitudes. Due to a fortunate combination of physical size and rotational phase of the unit, the thermal inertia is comparably well constrained for unit 3, with respect to other units. For half of the studied co–latitude slabs, the existence of a small thermal inertia can be *consistently* excluded at a 99% confidence level, with lower limits ranging between 500–1000 $\mathrm{J\,m^{-2}\,K^{-1}\,s^{-1/2}}$. We therefore feel confident that the thermal inertia of unit 3 is rather large, and this conclusion should be immune to possible HRI–IR calibration errors.

For unit 4, the $Q \geq 0.01$ error bars are too large to allow any meaningful constraint on the thermal inertia (this is also true for $Q \geq 0.317$). However, if the $\min(\chi^2)$ solutions corresponding to the largest (most reliable) H–values are considered (see Fig. 8), an average $\langle \mathcal{I} \rangle = 2400 \pm 1300\,\mathrm{J\,m^{-2}\,K^{-1}\,s^{-1/2}}$ is obtained, which is comparable to the likely thermal inertia of units 1 and 3. If we accept the theory that unit 5 is less rough than units 1, 3, and (possibly) 4, the $\min(\chi^2)$ solutions corresponding to the largest H–values for that unit yield $\mathcal{I} = 10$–$200\,\mathrm{J\,m^{-2}\,K^{-1}\,s^{-1/2}}$, with an average of $\langle \mathcal{I} \rangle = 60\,\mathrm{J\,m^{-2}\,K^{-1}\,s^{-1/2}}$. Although very uncertain, this shows that the morphological units on Comet 9P/Tempel 1 possibly have very different physical properties.

As mentioned previously, the data on unit 6 is scarce and the results are unreliable. If the $\min(\chi^2)$ solutions are considered, they indicate a very low thermal inertia, ranging between

$\mathcal{I} = 10$–$90\,\mathrm{J\,m^{-2}\,K^{-1}\,s^{-1/2}}$, with an average of $\langle\mathcal{I}\rangle = 40\,\mathrm{J\,m^{-2}\,K^{-1}\,s^{-1/2}}$. The northern part of unit 7 have $\min(\chi^2)$ solutions consistently in the range $\langle\mathcal{I}\rangle = 380 \pm 150\,\mathrm{J\,m^{-2}\,K^{-1}\,s^{-1/2}}$, while the southern part displays a substantial scatter of $\min(\chi^2)$ estimates (covering $\mathcal{I} = 10$–$3000\,\mathrm{J\,m^{-2}\,K^{-1}\,s^{-1/2}}$, with an average of $\langle\mathcal{I}\rangle = 1000\,\mathrm{J\,m^{-2}\,K^{-1}\,s^{-1/2}}$). Units 6 and 7 both have $Q \geq 0.01$ thermal inertia error bars covering the entire considered range, except for two co–latitude slabs in unit 7 centered on $l_{\mathrm{co}} = 142°$ and 146° where $\mathcal{I} \geq 400\,\mathrm{J\,m^{-2}\,K^{-1}\,s^{-1/2}}$. If 1–$\sigma$ error bars are considered instead, a thermal inertia below 150–200 $\mathrm{J\,m^{-2}\,K^{-1}\,s^{-1/2}}$ can additionally be excluded at a 68.3% confidence level for unit 7 at $120° \lesssim l_{\mathrm{co}} \lesssim 140°$.

3.3 Interpretation of the Surface Roughness

We here apply the circular paraboloid pit model described in Sec. 2.3 to give a possible geometrical interpretation of the small scale self heating parameter ξ estimated in Sec. 3.2. Although the model is arbitrarily chosen (and hence may not be a good representation of reality), we still consider it important to express the rather abstract parameter ξ in terms of quantities that are easier to visualize (area coverage f of pits with depth–to–diameter ratio S).

As seen from Eq. (20), an empirically estimated ξ–value only leads to the specification of a relation $f = f(S)$, i.e., f and S cannot be disentangled. We here consider the ξ values corresponding to the most likely solutions X for each co–latitude slab. To further simplify the problem, we here focus on the smallest depth–to–diameter ratio S_{min} (and hence, largest area coverage $f(S_{\mathrm{min}})$) consistent with locally estimated ξ values. It should therefore be remembered that the estimated areal coverage of pits could be smaller than given here, in case the pits are deeper with more narrow entrances and/or if the most likely X value in fact is too small.

The upper and lower panels of Fig. 10 show how S_{min} and $f(S_{\mathrm{min}})$ vary across the nucleus disk, respectively. For unit 1 (thin layers terrain), the average parameters are $\langle S_{\mathrm{min}}\rangle = 1.0$ and $\langle f(S_{\mathrm{min}})\rangle = 91\%$, while unit 3 (scarped/pitted terrain) has the same area coverage but somewhat deeper pits, $\langle S_{\mathrm{min}}\rangle = 1.2$. The two units are therefore rather similar, and neither unit displays large internal variations in S_{min} or $f(S_{\mathrm{min}})$. Unit 4 (thick layers terrain) has a similar area coverage

of $\langle f(S_{\rm min})\rangle = 93\%$, and deeper pits still, $\langle S_{\rm min}\rangle = 1.5$. Note that the southmost part of the boundary area between units 3 and 4 appears particularly rough.

As mentioned previously, unit 5 (thin layers terrain) appears smoother than units 1, 3, and 4, which is reflected in the more modest average pit coverage $\langle f(S_{\rm min})\rangle = 62\%$, and the substantially shallower pits, $\langle S_{\rm min}\rangle = 0.4$. For unit 6 (smooth terrain) the parameters are highly uncertain, with values $\langle f(S_{\rm min})\rangle = 87\%$ and $\langle S_{\rm min}\rangle = 1.2$. It may seem a paradox that unit 6, which looks very smooth compared to, e.g., unit 3 on visible images, appears almost equally rough in the current analysis. However, it must be remembered that we here deal with subpixel roughness, which may be similar for units that have very different global topographic properties. Furthermore, the physical size of pits with the same S–value may be very different and could in principle be systematically smaller for one unit with respect to others.

The northern part of unit 7 (scarped/pitted terrain) has shallow pits ($\langle S_{\rm min}\rangle = 0.5$) similar to those of unit 5 but a somewhat higher area coverage ($\langle f(S_{\rm min})\rangle = 74\%$). The southern part of unit 7 has the most extreme pits on the visible side of the nucleus, $\langle S_{\rm min}\rangle = 1.6$ and the area coverage is rather high, $\langle f(S_{\rm min})\rangle = 91\%$.

The current study suggests that the surface irregularity that clearly is visible on global scales, also is present on subpixel scales – the surface does not turn flat on size scales below ~ 60 m. This should not come as a surprise, due to the low surface gravity of 9P/Tempel 1. Due to surface roughness the capability of surface elements within locally convex geometries to dissipate heat into space is reduced, which leads to an overall temperature increase of the surface material due to self heating. The small scale self heating parameter ξ needed in order to reproduce the empirical temperature profiles $T_{\rm emp}(t)$ is rather high. However, the geometric surface conditions required to produce such ξ–values are not excessively extreme. Pits with roughly the same depth as their diameters, covering as little as $\sim 60\%$ or as much as $\sim 90\%$ of the surface are sufficient to explain the estimated level of self heating.

3.4 Properties of the Surface Material

As mentioned in Sec. 2.3, the circular paraboloid model may be used to calculate a numerical beaming function $\Lambda = \Lambda(S,\, f,\, \mu_{\rm e},\, \gamma)$. Combined with the directional emissivity $\varepsilon_{\rm d}$ given by Hapke (1993) it yields Eq. (22), i.e., a modeled version of X' called $X'_{\rm mod}$. Here, X' is the correction to the Planck function needed to account for macroscopic topography as well as having surface material not behaving as a black–body. The parameter X' is obtained directly from the HRI–IR spectra and seen in the upper right panel of Fig. 3. For each HRI–IR pixel, an average (cosine of) emission angle $\mu_{\rm e}$ can be assigned from the shape model, and the estimated ξ value yields a relation $f = f(S)$ that limits the functional dependence of $X'_{\rm mod}$ to two parameters, S and γ. Fortunately, $X'_{\rm mod}$ is virtually independent on S, why matching of X' and $X'_{\rm mod}$ yields an estimate of γ, which trivially yields the volume emissivity factor γ^2.

A map of γ^2 is seen in the lower right panel of Fig. 3. Note that areas in black show pixels removed due to shadowing and/or global self heating problems. As can be seen, units 1, 4, 5, 6, and the northern part of unit 7 generally have very high γ^2 values – in fact, the median values are $\langle\gamma^2\rangle_{\rm med} = 1.0$ in all cases. The mean values for these units cover the range $0.79 \leq \langle\gamma^2\rangle_{\rm mean} \leq 0.95$. From Eq. (23) this suggests that the constituent particles covering most of the surface of these units are good absorbers of radiation at $3.0 \leq \lambda \leq 3.6\,\mu$m, and equivalently, poor scatterers of such radiation.

However, unit 3 and the southern part of unit 7 (the scarped/pitted terrains) have volume emissivity factors that often are substantially smaller than unity. In fact, the median values are $\langle\gamma^2\rangle_{\rm med} = 0.36$ for unit 3 and $\langle\gamma^2\rangle_{\rm med} = 0.81$ for the south part of unit 7, while the corresponding mean values are $\langle\gamma^2\rangle_{\rm mean} = 0.44$ and $\langle\gamma^2\rangle_{\rm mean} = 0.69$. The constituent particles of unit 3 and the southern parts of unit 7 therefore appear to behave differently with respect to surface particles in the other units – the grains are rather poor absorbers of radiation at $3.0 \leq \lambda \leq 3.6\,\mu$m, but rather efficient scatterers of such radiation.

We here speculate about possible reasons for those differences. However, first we attempt to place constraints on the typical grain size in the surface material. For this purpose, model

hemispherical emissivities $\varepsilon_{\rm h,mod}$ as functions of wavelength have been calculated according to Eq. (24), using γ–values obtained for a number of grain radii a from Mie modeling of the substances discussed in Sec. 2.4. The results for selected species are seen in Fig. 11. Note specifically, that all the considered species (for a wide range of grain sizes, $0.01\,\mu{\rm m} \leq a \leq 100\,\mu{\rm m}$) have $0.8 \lesssim \varepsilon_{\rm h,mod} \lesssim 1.0$ for $\lambda \gtrsim 10\,\mu$m (except for 5–10 μm grains of carbon). This is consistent with the standard assumption in comet thermophysics literature that the "emissivity ε" in the vicinity of the Wien peak is near $\varepsilon \approx 0.9$. However, it is also clear that iron–poor silicates have substantially smaller emissivities at shorter wavelengths. Hence, it is not recommendable to assume emissivities near unity when analyzing emission spectra at $\lambda \lesssim 5.0\,\mu$m. Fig. 11

Applying Eq. (25), the curves in Fig. 11 may be used to calculate the integrated emissivity $\overline{\varepsilon}_{\rm h,mod}$ (here using $250 \leq T \leq 350\,{\rm K}$), from which a modeled bolometric albedo $A_{\rm mod} \approx 1 - \overline{\varepsilon}_{\rm h,mod}$ is estimated (see Appendix B). This modeled bolometric albedo may be compared to the value $A \approx A_{\rm v} = 0.013 \pm 0.002$ measured by Li et al. (2007) (see Table 2). As it turns out, $A_{\rm mod}$ increases rapidly with grain size. For all the considered species (and temperatures), $0.005 \leq A_{\rm mod} \leq 0.012$ when $a = 0.1\,\mu$m, while even smaller grain sizes reduce $A_{\rm mod}$ further. It is also found that $0.017 \leq A_{\rm mod} \leq 0.091$ for all considered species and temperatures when $a = 0.5\,\mu$m, while even larger grain sizes increases $A_{\rm mod}$ further. It therefore appears reasonable, that the measured value $A = 0.013 \pm 0.002$ limits the size range for the majority of the particles in the surface material to $0.1 \lesssim a \lesssim 0.5\,\mu$m. This estimate may be compared with the dust size distribution derived by Jorda et al. (2007) from OSIRIS/Rosetta imaging of the 9P/Tempel 1 dust cloud formed by the DI impact experiment. They find that the overwhelming majority ($\sim 80\%$) of the grains in the ejecta cloud (in terms of cross section, which is the relevant measure also for us) had $a \leq 1.4\,\mu$m. With a differential size distribution power law index of 3.1 ± 0.3, as derived by Jorda et al. (2007), the $a \approx 0.1\,\mu$m and $a \approx 0.5\,\mu$m grains should outnumber the $a \approx 1.4\,\mu$m grains by roughly three and one orders of magnitude, respectively. For the sake of simplicity, we therefore limit the following discussion to particles of size $0.1 \leq a \leq 0.5\,\mu$m. Fig. 12

Remembering that the lower right panel of Fig. 3 shows the estimated γ^2 values for the nucleus

at $3.0 \leq \lambda \leq 3.6\,\mu$m, we now consider a wavelength near the center of that interval, $\lambda = 3.25\,\mu$m. Figure 12 shows $\gamma^2_{\rm mod}$ as a function of grain size $0.01 \leq a \leq 50\,\mu$m at $\lambda = 3.25\,\mu$m, for the species considered in this study. Note that the size interval $0.1 \leq a \leq 0.5\,\mu$m, which we find particularly important, is marked by vertical dotted lines. For units 1, 4, 5, 6, and the northern part of unit 7 we obtained median values $\langle\gamma^2\rangle_{\rm med}$ of unity, and mean values above ~ 0.8. In order to obtain such values with the currently considered minerals, it is necessary to focus on the smallest possible grains, in this case $a \approx 0.1\,\mu$m. Furthermore, species with inefficient absorptivity, such as iron–poor silicates and troilite are incapable of producing high enough volume emissivity factors. A highly absorbing material is needed, such as silicates with at least 50% iron abundance (with respect to the total metal content), or even better, carbon. Regarding the surface layer of units 1, 4, 5, 6, and the northern part of unit 7, our best guess is therefore that they primarily consist of $0.1\,\mu$m grains of iron–rich silicates and/or organic material – or minerals with similar optical properties at $3.0\,\mu{\rm m} \leq \lambda \leq 3.6\,\mu$m.

For unit 3 and the southern part of unit 7, we found relatively low volume emissivity factors, with mean values in the range $0.44 \leq \langle\gamma^2\rangle_{\rm mean} \leq 0.69$. Figure 12 shows that small ($a \sim 0.1\,\mu$m) grains may reproduce such low values, but only if consisting of material with low absorptivity, such as iron–poor silicates or troilite. It is also clear that large ($a \sim 0.5\,\mu$m) grains readily yield the sought–for low volume emissivity factors, regardless of composition.

It therefore appears reasonable that units 3 and the southern part of unit 7 consist of grains which are fundamentally different from those covering the remainder of the nucleus. One possibility is that the entire nucleus is covered by iron–rich silicate and/or organic material, but that units 3 and the southern part of unit 7 have systematically larger grains than other units, i.e., chemical homogeneity but physical heterogeneity. A second possibility is that the typical grain size is the same in all locations (by necessity small, $a \approx 0.1\,\mu$m), but that units 3 and the southern part of unit 7 have a different composition (e.g., being richer in iron–poor silicates and troilite) compared to the remainder of the nucleus (which may be dominated by organic material and iron–rich silicates), i.e., chemical heterogeneity but physical homogeneity. A third possibility is of course

that both chemical and physical properties differ between units – the only thing we may exclude is that the entire nucleus surface material is chemically and physically homogeneous.

4 Discussion

4.1 Comparison with Previous Work

4.1.1 Reddening

To our knowledge, the present investigation of spatially resolved spectral reddening at $1.2 \leq \lambda \leq 2.5\,\mu$m for the nucleus of Comet 9P/Tempel 1 is unique. The perhaps most interesting result is that unit 2 has the lowest degree of reddening of any unit. Li et al. (2007) also found that this particular region has the lowest $0.75\,\mu$m–to–$0.55\,\mu$m color ratio on the nucleus. Combining these two discoveries consistently shows that unit 2 spectrally is more neutral than other visible parts of the nucleus, for a large wavelength region covering at least $0.55\,\mu\text{m} \leq \lambda \leq 2.5\,\mu$m. Interestingly, the other smooth area on the nucleus, unit 6, is found to be redder than average in both investigations. We consider these consistencies a sign of credibility for our R fitting procedure. However, we also note that the surge in reddening seen for unit 4 in our data, does not appear to have an optical counterpart. The reason why the level of spectral reddening varies across the nucleus disk, and why optical and near–infrared spectral slopes behave similarly in some regions while differing in others, is unclear. Possible explanations include differences in chemical composition, degree of space weathering, or grain size distribution across the surface, or a combination of such factors. We consider the apparent correlation between reddening and morphological units particularly interesting, as it may suggest that regions with different global characteristics (in terms of topography, layering, *et cetera*) also differ measurably in terms of chemical and micro–physical properties, perhaps including space weathering exposure ages. This could in turn be useful when trying to reconstruct the evolutionary history of this comet nucleus.

4.1.2 Roughness

Regarding small scale surface roughness, we find that a substantial fraction of the nucleus (units 1, 3, 4, 6, and southern part of 7) has a rather uniform high roughness, with best fit unit averages ranging $0.61 \leq \langle\xi\rangle \leq 0.75$. Locally, the roughness may increase above $\xi \approx 0.8$, particularly near the southmost boundary between units 3 and 4, as well as in the southern part of unit 7. Unit 5 and the northern part of unit 7 (forming a physically coherent area) appear smoother than the rest of the nucleus, with best fit unit averages of $0.23 \leq \langle\xi\rangle \leq 0.33$.

These results on roughness, based on thermophysical model reproduction of temperatures extracted from the near–infrared spectrum, should be compared with findings from Hapke modeling of the disk–resolved visible photometry performed by Li et al. (2007). However, such a comparison requires that a representative ξ value from the current work is translated to a corresponding Hapke roughness parameter, the mean slope angle $\bar{\theta}$. Here, this is done by considering a thin azimuthal slice of a $S = 1$ circular paraboloid pit and obtaining the distribution $D(\theta)$ of area weighted angles θ between local surface normals and the paraboloid symmetry axis, normalized according to Eq. (4) in Hapke (1984). This distribution is then inserted into Eq. (5) in Hapke (1984), which defines $\bar{\theta}$ as,

$$\tan\bar{\theta} = \frac{2}{\pi}\int_0^{\pi/2} \tan\theta\, D(\theta)\, d\theta. \tag{26}$$

Correcting $\bar{\theta}$ for a typical $f = 90\%$ coverage of pits, we then obtain $\bar{\theta} \approx 55°$.

According to Li et al. (2007), the roughness does not vary strongly for the bulk of the nucleus surface, and they obtain an average Hapke roughness parameter of $\bar{\theta} = 16° \pm 8°$. However, they do point out that the southern part of unit 7 is measurably rougher than the rest of the nucleus, and obtain $\bar{\theta} = 32° \pm 9°$ for that region. Furthermore, an area which is either brighter or smoother than average is discussed by Li et al. (2007). It is characterized by moderate to high incidence angles i and low to moderate emission angles e ($i \gtrsim 45°$ and $e \lesssim 45°$ according to their Fig. 5). Li et al. (2007) consider unit 6 the best candidate, "where the roughness parameter should be lower than average." However, smooth global topography is not a guarantee for a low degree of small scale surface roughness, and we point out that the nearby unit 5 has virtually the same

average emission angle as unit 6 ($\langle e \rangle_{\rm mean} = 48^\circ$ for unit 5 and $\langle e \rangle_{\rm mean} = 43^\circ$ for unit 6), and only a somewhat smaller average incidence angle ($\langle i \rangle_{\rm mean} = 42^\circ$ for unit 5 and $\langle i \rangle_{\rm mean} = 61^\circ$ for unit 6). We therefore propose that the supposedly smooth area actually may be part of unit 5 rather than unit 6.

We therefore consider our results qualitatively similar to those of Li et al. (2007), in the sense of having a rather uniform degree of roughness for a substantial fraction of the surface, higher than average roughness for the southern part of unit 7, and *possibly* a smaller than average roughness of unit 5. However, the quantitative consistency is a more delicate problem, since our typical $\bar{\theta}$ value is substantially larger than those reported by Li et al. (2007).

A possible explanation for the discrepancy may be that the two different methods measure $\bar{\theta}$ at fundamentally different size scales. The size scale predominantly contributing to $\bar{\theta}$–values obtained in Hapke modeling of visual photometric data is a matter of substantial uncertainty. Formally, $\bar{\theta}$ should sample all size scales from a few grain radii to structures just under the instrument resolution limit (roughly $\sim 80\,$m with the 4×4 binned HRI visual images used by Li et al. (2007)). Some investigations (e.g., Helfenstein 1988) lend support to that idea. However, there are also several works indicating that $\bar{\theta}$ predominantly measures roughness on physically small scales. Shepard and Campbell (1998) argued that the photometric roughness measured by $\bar{\theta}$ is dominated by the smallest size scale for which shadows still exist – which is a few times the wavelength of incident radiation if diffraction dominates shadow removal ($\sim 1\,\mu$m), although it could be substantially larger (centimeters) if shadows are removed by efficient multiple scattering (a mechanism which decreases in importance when $A_{\rm v}$ is reduced). In this context it is interesting that $\lesssim 5\%$ of the roughness measured for lunar regolith originates from topographic features larger than $\sim 8\,$cm according to Helfenstein and Shepard (1999). In their laboratory investigation of regolith analogues, Cord et al. (2003) found that $\bar{\theta}$ primarily was determined by roughness on the sub–mm to cm level. Similar conclusions were drawn by Shepard and Helfenstein (2007), who derived $6^\circ \leq \bar{\theta} \leq 31^\circ$ from Hapke analysis of reflectance spectra of compacted sand samples, which completely lacked topography at $\gtrsim 1\,$mm scales. In this case, the $\bar{\theta}$–value was therefore sensitive

to roughness on grain size level, but insensitive to the macroscopic topography (otherwise $\bar{\theta}$ would have been substantially lower).

Hence, if the Hapke roughness parameter obtained by Li et al. (2007) predominantly measures topography on size scales below a few centimeters, one may imagine a particulate surface which essentially is smooth on that scale, but still could have substantial topographic features (e.g., pits) on the scales of decimeters, meters, and tens of meters. On scales of centimeters and smaller, self heating would be fairly insignificant since $\bar{\theta} = 16^\circ \pm 8^\circ$ corresponds to $0.03 \lesssim \xi \lesssim 0.16$ for a surface with a Gaussian slope distribution (Lagerros 1997). This lateral radiative transport mechanism would be complementary to, and perhaps practically indistinguishable from, lateral solid state heat conduction, acting on size scales comparable to the thermal skin depth (a couple of decimeters for particulate enstatite with $\psi = 0.4$). However, on size scales of decimeters and larger, self heating could be very important, if the surface on such scales is characterized by $\xi \approx 0.7$. The later comparably large scale topography could go virtually undetected in standard Hapke modeling, but would dominate the self heating detectable when modeling surface temperatures.

Another possible reason for the difference in $\bar{\theta}$ between Li et al. (2007) and the present investigation is related to the inherent assumption in the Hapke (1984) theory that the mean slope $\bar{\theta}$ of an observed surface is small. Specifically, the slope distribution of a surface is taken to be a Gaussian,

$$D(\theta) = \mathcal{A} \exp\left(-\frac{\tan^2\theta}{\mathcal{B}}\right) \frac{\sin\theta}{\cos^2\theta}, \tag{27}$$

and it is assumed that the parameters $\mathcal{A}$ and $\mathcal{B}$ are given by the following approximate expressions,

$$\mathcal{A} \approx \frac{2}{\pi \tan^2\bar{\theta}} \tag{28}$$

$$\mathcal{B} \approx \pi \tan^2\bar{\theta}, \tag{29}$$

which is the point where the small–$\bar{\theta}$ assumption is introduced. The suitability of Eqs. (28) and (29) can easily be investigated by assuming a certain $\bar{\theta}$ (the "input mean slope", henceforth $\bar{\theta}_{\rm i}$), evaluate Eq. (27) for the corresponding values of $\mathcal{A}$ and $\mathcal{B}$, and insert the resulting distribution $D(\theta)$ into Eq. (26) to see if the assumed $\bar{\theta}$ indeed is recovered (the "output mean slope", henceforth

$\bar{\theta}_{\rm o}$). One then finds that $\bar{\theta}_{\rm o} \approx \bar{\theta}_{\rm i}$ when $\bar{\theta}_{\rm i}$ is small, but as $\bar{\theta}_{\rm i}$ grows, Eqs. (28)–(29) rapidly break down. For example, if $\bar{\theta}_{\rm i} = 10^\circ$ then $\bar{\theta}_{\rm o} = 9.4^\circ$, but if $\bar{\theta}_{\rm i} = 30^\circ$ then $\bar{\theta}_{\rm o} = 21.2^\circ$. If one has a surface with a mean slope $\bar{\theta}_{\rm i} = 55^\circ$ (e.g., 90% of an otherwise flat surface punctuated by circular paraboloid pits with diameter–to–depth ratio near unity), the slope distribution $D(\theta)$ supposed to represent this surface according to Hapke theory, e.g., Eqs. (27)–(29), only yield an actual mean slope of $\bar{\theta}_{\rm o} = 28.3^\circ$ according to Eq. (26). In fact, as $\bar{\theta}_{\rm i} \rightarrow 90^\circ$, we have $\bar{\theta}_{\rm o} \rightarrow 32.5^\circ$. We note that none of the fitted $\bar{\theta}$–values compiled by Cord et al. (2003) for 16 Solar System bodies (including an average for S–asteroids) exceeds 36°, and find the near coincidence with the upper limit on $\bar{\theta}_{\rm o}$ interesting.

4.1.3 Thermal inertia

Generally, it is very difficult to constrain the thermal inertia of Comet 9P/Tempel 1. The reason is mainly that a low χ^2 often can be found when the thermal inertia is relatively low as long as the X–value simultaneously is relatively high – and vice versa. The range in X resulting from this coupling is relatively small (i.e., it can be fairly well constrained), but this is not the case for the thermal inertia. With the current 3–σ error bars, virtually any considered value of $\mathcal{I}$ may yield a reasonable reproduction of the empirical data (if X is chosen carefully). If 1–σ error bars are used, it is somewhat easier to exclude a thermal inertia below a few hundred $\mathrm{J\,m^{-2}\,K^{-1}\,s^{-1/2}}$ for individual co–latitude slabs in units 1 and 7, but it does not lead to dramatically tighter overall constraints. Although rather unsatisfactory a result, this may still be an important discovery, since it invalidates earlier claims that the thermal inertia of Comet 9P/Tempel 1 *by necessity* must be very low. We also note that the situation would improve substantially, if the temperature uncertainty could be reduced to, say ±2–3 K. For future spacecraft missions, we strongly recommend to aim for temperature uncertainties of at most ±3 K, which would allow us to disentangle X and $\mathcal{I}$.

The exception to the general uncertainty in thermal inertia is unit 3, where we consider $\mathcal{I} \geq$ 500–1000 $\mathrm{J\,m^{-2}\,K^{-1}\,s^{-1/2}}$ not only possible but *necessary* in order to explain the empirical data. The HRI–IR data shows relatively high morning temperatures and that a gradual temperature

increase is taking place in areas where the cosine of the solar zenith angle increases rapidly (e.g., Fig. 4). Both features are tell–tale signs of a surface material having a substantial thermal inertia. Heat conducted into the nucleus during daytime is keeping the surface warm during nighttime, and at local daybreak the surface is still rather hot. The surface material does not reply instantly to increments in solar illumination flux, but in a gradual manner which is indicative of ongoing heat conduction.

In case the $\min(\chi^2)$ solutions indeed correspond well to reality, our best guess is that units 1, 3, 4, and the southern part of unit 7 have rather high thermal inertia, typically $\mathcal{I} = 1000$–$3000\,\mathrm{J\,m^{-2}\,K^{-1}\,s^{-1/2}}$, while unit 5, 6, and the northern part of unit 7 have considerably smaller thermal inertia, typically $\mathcal{I} \lesssim 380\,\mathrm{J\,m^{-2}\,K^{-1}\,s^{-1/2}}$. These results are partially contradicting Groussin et al. (2007), who considered $\mathcal{I} \lesssim 50\,\mathrm{J\,m^{-2}\,K^{-1}\,s^{-1/2}}$ necessary to reproduce the HRI–IR data. However, their conclusion may be strongly biased by only considering models with $X = 0.9$, as explained in the following.

The lower panel of Fig. 4 illustrates why models neglecting surface roughness lead to extremely low thermal inertia estimates. The area in $\{X, \mathcal{I}\}$ parameter space where χ^2 is relatively small is traced by the dots in that panel and form a curve we may denote $X_\star = X_\star(\mathcal{I})$. At large thermal inertia, the $X_\star$ curve is virtually horizontal, but as the thermal inertia decreases below a few hundred $\mathrm{J\,m^{-2}\,K^{-1}\,s^{-1/2}}$, the $X_\star$ curve rapidly turns upward. If a thermophysical model is used which exclusively considers $X = 0.9$, we are limited to a horizontal line in $\{X, \mathcal{I}\}$ space which never intersects the $X_\star$ curve. The only region where we are anywhere near the $X_\star$ curve is at $\mathcal{I} \approx 0$. For example, the upper panel of Fig. 4 shows the $X = 0.9$ model with the smallest χ^2–value (obtained for $\mathcal{I} = 10\,\mathrm{J\,m^{-2}\,K^{-1}\,s^{-1/2}}$), as a dotted curve. It is in fact far below the $T_{\mathrm{emp}}(t)$ curve and is inconsistent with the empirical data. It should be remembered that differences in the methods used to extract the empirical temperature (treatment of X' in Eq. (4)) are by far not large enough to bridge the gap between measurements and the dotted curve.

Models neglecting self heating caused by surface roughness are simply too cold with respect to the observations, even when (cooling) energy loss into the interior is switched off completely

by letting $\mathcal{I} \to 0$. We believe this explains the statement by Groussin et al. (2007), who only considered $X = 0.9$ (see their Fig. 5); "To first order, the model agrees with the data only for very low values of thermal inertia. The fit is not perfect. [...] However, even if the fit is not very good, the fit gets worse as the thermal inertia increases."

4.1.4 Porosity of the dust mantle

In case the $\min(\chi^2)$ solutions reflect physical reality, our best guess is that units 1, 3, 4, and the southern part of unit 7 have rather high thermal inertia, typically $\mathcal{I} = 1000$–$3000\,\mathrm{J\,m^{-2}\,K^{-1}\,s^{-1/2}}$. Is such a high thermal inertia consistent with the current paradigm that comet material is highly porous? If the model described at the end of Sec. 2.2 is used, we find that a thermal inertia of $\mathcal{I} = 1000$–$3000\,\mathrm{J\,m^{-2}\,K^{-1}\,s^{-1/2}}$ is expected for pulverized silicate material (enstatite and forsterite mixture) if the porosity is $0.20 \leq \psi \leq 0.59$. The lower value is near the close–packing limit of equal–sized spheres, and the higher value is near the bulk porosity estimated for comets, $\psi = 0.6 \pm 0.3$ (Davidsson 2006). The upper limit is also just below the range $0.67 \leq \psi \leq 0.8$ expected for grain agglomerates formed by random ballistic deposition, mildly compacted by collisions during planetesimal formation (Blum et al. 2006). The thermal inertia we obtain for unit 3 is therefore not unrealistically high – on the contrary, it is actually close to the values we would expect for silicate dust mantle material with medium to high porosity.

If our best estimates for units 5, 6, and the northern part of unit 7 are considered ($\mathcal{I} = 40$–$380\,\mathrm{J\,m^{-2}\,K^{-1}\,s^{-1/2}}$), such values are obtained for porosities $0.72 \leq \psi \leq 0.85$. These values are high to very high and can be compared with estimates for the DI impact site, located within unit 5. Ernst and Schultz (2007) compared the impact flash behavior with results from laboratory impact experiments and concluded the porosity was $0.75 \leq \psi \leq 0.88$ at the impact site. For unit 5 we estimate $\psi \approx 0.85$, based on the average thermal inertia of $\langle\mathcal{I}\rangle = 60\,\mathrm{J\,m^{-2}\,K^{-1}\,s^{-1/2}}$ and the model of porosity–dependence of thermal inertia presented at the end of Sec. 2.2. These results are in perfect agreement, which may indicate that our method (including the arguments presented regarding Fig. 8 as well as the applied porosity model) is reliable.

4.1.5 Density of the dust mantle

Using a density $\rho_{\rm comp} = 3275\,{\rm kg\,m^{-3}}$ of compacted surface material (Sec. 2.2) and a porosity of $0.20 \leq \psi \leq 0.59$ yields a dust mantle density of $1300 \lesssim \rho \lesssim 2600\,{\rm kg\,m^{-3}}$ for the regions with an estimated high thermal inertia (units 1, 3, 4, and the southern part of unit 7). This range can be compared to densities derived from dielectric constants obtained in radar observations of comet nuclei (Harmon et al. 2004, 2008). Assuming a silicate powder covering the nucleus, one then obtains $\rho \approx 900\,{\rm kg\,m^{-3}}$ for C/1983 H1 (IRAS–Araki–Alcock), $\rho \approx 1200\,{\rm kg\,m^{-3}}$ for 2P/Encke, $\rho \approx 1300\,{\rm kg\,m^{-3}}$ for 26P/Grigg–Skjellerup, $\rho \approx 1500\,{\rm kg\,m^{-3}}$ for C/1983 J1 (Sugano–Saigusa–Fujikawa), and $\rho \approx 1800\,{\rm kg\,m^{-3}}$ for 8P/Tuttle. All five objects have surface bulk densities near or within the considered interval (with a preference for the lower half). Provided that the method used to convert thermal inertia to porosity and bulk density is acceptable, our best fit $\mathcal{I}$ values for 9P/Tempel 1 therefore seem consistent with radar measurements obtained for several other comets. Hence, our mathematically preferred solutions cannot be disregarded as being physically implausible, since it is not unrealistic to have a substantial fraction of the nucleus surface covered by devolatilized silicate material.

Using the same compacted density $\rho_{\rm comp} = 3275\,{\rm kg\,m^{-3}}$, but a porosity of $0.72 \leq \psi \leq 0.85$, yields a plausible dust mantle density of $500 \lesssim \rho \lesssim 900\,{\rm kg\,m^{-3}}$ for units 5, 6, and the northern part of unit 7. This shows that there may be a substantial heterogeneity in dust mantle density over the comet nucleus surface. Some regions may have a rather loose structure, resulting in low density and low thermal inertia. The solid particles in these regions may be gardened and broken up by upwelling gas from below. Belton and Melosh (2008) have suggested that the smooth terrains (e.g., unit 6) in fact are landslides, caused by fine–grained material being fluidized by CO and CO_2 and flowing virtually frictionless down gravitational gradients. It may therefore not be surprising that we find low thermal inertia and density for unit 6, and the "downstream" units 5 and 7 (the northern part).

However, other regions may have a substantially more compact and cemented structure, resulting in a much higher density and thermal inertia. These regions may have been devolatilized a

long time ago, and there may not be enough gas welling up from the deep interior to loosen up the near–surface material. The porosity might gradually decrease as grains of minerals and organics settle into increasingly compact configurations, perhaps assisted by micro–vibrations by geological events taking place elsewhere. This material could consolidate further due to the presence of tar–like organics. As shown experimentally by Kömle et al. (1996), mixtures of silicate dust and organics develop into cohesive mantles upon solar heating, with substantially higher conductivity and thermal inertia than pure silicate powder. The reason is that plastically flowing organic material fill in gaps between the dust grains, building up sinter necks and connecting previously separated parts of the porous medium with each other. We suggest that units 1, 3, 4, and the southern parts of unit 7 could have been subjected to such cementation, hence explaining the high thermal inertia we believe to have found for these regions.

It should be emphasized that one must carefully distinguish between the density in a near–surface layer (that may be subjected to solar–driven evolutionary processes), and the *bulk density* of the entire nucleus, which is determined by the conditions in the deep interior. Using different techniques, Richardson et al. (2007) and Davidsson et al. (2007) both came to the conclusion that the bulk density of Comet 9P/Tempel 1 is near $\rho_{\rm bulk} \approx 400\,{\rm kg\,m^{-3}}$. Such a low density should be the result of a particular chemical composition of the interior (i.e., a high concentration of low–density volatile species) and a degree of micro– and macro–porosity that may differ substantially from that found near the surface. Therefore, we see no contradiction of having a bulk density $\rho_{\rm bulk} \approx 400\,{\rm kg\,m^{-3}}$ for the nucleus as a whole, while the dust mantle has a density of $500 \lesssim \rho \lesssim 900\,{\rm kg\,m^{-3}}$ in some regions, while other regions may have values as high as $1300 \lesssim \rho \lesssim 2600\,{\rm kg\,m^{-3}}$. The dust mantle may constitute a skin on the nucleus, where the density varies between the nucleus bulk value and values being a factor 3–6 higher than the bulk.

4.1.6 Thermal inertia of other Solar System bodies

We have argued that a comet surface thermal inertia of $\mathcal{I} = 1000$–$3000\,{\rm J\,m^{-2}\,K^{-1}\,s^{-1/2}}$ is expected from first principles (considering reasonable dust mantle analogue materials and porosities), and

is consistent with the rather compact comet surfaces revealed by radar observations. However, the small but growing number of thermal inertia estimates made for asteroids are typically below that range, which is concerning. Focusing on Near Earth Asteroids (NEAs, which may be more similar to comets than the large main belt asteroids), estimates include $\mathcal{I} \approx 100\,\mathrm{J\,m^{-2}\,K^{-1}\,s^{-1/2}}$ for 2002 $\mathrm{NY_{40}}$ (Müller et al. 2004), $\mathcal{I} \approx 180 \pm 50\,\mathrm{J\,m^{-2}\,K^{-1}\,s^{-1/2}}$ for (1580) Betulia (Harris et al. 2005), $\mathcal{I} \approx 600$–$800\,\mathrm{J\,m^{-2}\,K^{-1}\,s^{-1/2}}$ for (25143) Itokawa (Müller et al. 2005, Müller 2007), $\mathcal{I} \approx 100$–$300\,\mathrm{J\,m^{-2}\,K^{-1}\,s^{-1/2}}$ for (33342) 1998 $\mathrm{WT_{24}}$ (Harris et al. 2007), $\mathcal{I} \approx 100$–$200\,\mathrm{J\,m^{-2}\,K^{-1}\,s^{-1/2}}$ for (433) Eros (Müller 2007), and $\mathcal{I} \approx 200$–$1200\,\mathrm{J\,m^{-2}\,K^{-1}\,s^{-1/2}}$ for (54589) YORP (Müller 2007).

Some of these estimates may, or may not, be sensitive to selection and quality of data, as illustrated by the case of (25143) Itokawa. Mueller et al. (2007) originally derived $\mathcal{I} \approx 350\,\mathrm{J\,m^{-2}\,K^{-1}\,s^{-1/2}}$, which later was updated to $\mathcal{I} \approx 700\,\mathrm{J\,m^{-2}\,K^{-1}\,s^{-1/2}}$ (Müller 2007) after exclusion of one data set and re–calibration of another. In other cases, estimates of effective diameters obtained as part of the analysis are at odds with diameters measured by radar (and estimated albedos may be inconsistent with the taxonomic type), as was the case for 2002 $\mathrm{NY_{40}}$, (1580) Betulia, and early studies of (25143) Itokawa. This also leads to doubts regarding the validity of the corresponding thermal inertia. For example, if the effective diameter of 2002 $\mathrm{NY_{40}}$ is forced to match diameters estimated by radar, the thermal inertia estimate increases from $\mathcal{I} \approx 100\,\mathrm{J\,m^{-2}\,K^{-1}\,s^{-1/2}}$ to $\mathcal{I} \approx 1000\,\mathrm{J\,m^{-2}\,K^{-1}\,s^{-1/2}}$ for an assumed prograde rotation, and to $\mathcal{I} \approx 3000\,\mathrm{J\,m^{-2}\,K^{-1}\,s^{-1/2}}$ if the rotation is retrograde (Müller et al. 2004). This illustrates that thermal inertia estimates potentially are highly sensitive to model assumptions regarding the spin state, particularly the sense of rotation. In addition, thermal inertia estimates may be sensitive to assumptions regarding the exact shape of the body, as well as model assumptions regarding surface roughness and small scale self heating. Avoiding mistakes when simultaneously solving for thermal inertia and surface roughness may be particularly difficult. We can only conclude that thermal inertia estimates not necessarily are absolute but may be model dependent, and this must be taken into consideration when comparing results obtained with different methods and models. Also, if the presence of organics is as important for the dust mantle thermal inertia as one might

suspect, it is perhaps not surprising that comets, at least for parts of their surfaces, have a higher thermal inertia than rocky asteroids covered by non–consolidated pure silicate regolith.

4.1.7 Surface composition

In Sec. 3.4 we found that vast regions on Comet 9P/Tempel 1 are covered by a material with a very high absorptivity at $3.0 \leq \lambda \leq 3.6\,\mu$m. We found that small ($a \approx 0.1\,\mu$m) grains of iron–rich silicates or carbon are good candidates. In this context, it is interesting to note that the DI collider impacted 9P/Tempel 1 within unit 5, in an area where we obtain $0.85 \leq \gamma^2 \leq 1.0$. If the dust ejecta is representative for the surface itself (which should not be taken for granted, since the ejecta contained material comprising several meters of near–surface material), we would therefore expect a concentration of strongly absorbing elements in the ejecta, such as iron–rich silicates and carbon. According to Lisse et al. (2007) the ejecta composition was 45% silicates (olivines, pyroxenes, and phyllosilicates), 30% organics (amorphous carbon and PAHs), 19% metal sulfides (dominated by troilite), and 6% carbonates, by (atomic/molecular) number. For silicates, the Fe/Mg abundance ratio was 0.77. Since $Mg_{0.6}Fe_{0.4}SiO_3$ with Fe/Mg = 0.67 has $\gamma^2 \approx 0.6$, and since $Mg_{0.4}Fe_{0.6}SiO_3$ with Fe/Mg = 1.5 has $\gamma^2 \approx 0.8$ according to Fig. 12 ($a = 0.1\,\mu$m grains at $\lambda = 3.25\,\mu$m), a reasonable bulk volume emissivity factor for the silicates in the ejecta would be $\gamma^2 \approx 0.62$. Applying the same value for troilite as for silicates, and using $\gamma^2 \approx 1$ for carbon, the weighted average for the ejecta (ignoring carbonates) is then $\gamma^2 \approx 0.74$. This is somewhat low compared to $0.85 \leq \gamma^2 \leq 1.0$, but we note the estimate $\gamma^2 \approx 0.74$ would increase, e.g. if the organic material partially is encapsulating the silicates. We therefore do not see any strong reason to doubt our γ^2 values obtained for unit 5, given the observed properties of the ejecta.

4.2 Global Characterization of Comet 9P/Tempel 1

We here summarize the results obtained for each morphological unit to facilitate a cross–comparison and analysis. We focus on presenting unit averages of best fit values and due to the previously discussed error bars we emphasize that apparent differences between morphological units not nec-

essarily are statistically significant. We also emphasize that the nucleus may not be composed of the specific minerals discussed here. Other minerals may be present, having similar optical properties to the ones we studied.

• *Unit 1.* Thin layers terrain with comparatively low reddening, $\langle R \rangle = 3.3\,\%\,\mathrm{k\AA}^{-1}$. Rough surface with $\langle X \rangle \approx 0.35$ and $\langle \xi \rangle \approx 0.65$ (e.g., 91% coverage of $S = 1.0$ pits). Probably high thermal inertia around $\langle \mathcal{I} \rangle \approx 2500\,\mathrm{J\,m^{-2}\,K^{-1}\,s^{-1/2}}$, corresponding to a porosity $\langle \psi \rangle \approx 30\%$. The unit may be composed of small ($a \approx 0.1\,\mu\mathrm{m}$) grains of iron–rich silicates and carbon ($\langle \gamma^2 \rangle_{\mathrm{med}} = 1$).

• *Unit 2.* Smooth terrain with the lowest measured average reddening, $\langle R \rangle = 3.2\,\%\,\mathrm{k\AA}^{-1}$.

• *Unit 3.* Scarped/pitted terrain with comparatively low reddening, $\langle R \rangle = 3.3\,\%\,\mathrm{k\AA}^{-1}$. Rough surface with $\langle X \rangle \approx 0.28$ and $\langle \xi \rangle \approx 0.73$ (e.g., 91% coverage of $S = 1.2$ pits). Probably high thermal inertia around $\langle \mathcal{I} \rangle \approx 1900\,\mathrm{J\,m^{-2}\,K^{-1}\,s^{-1/2}}$, corresponding to a porosity $\langle \psi \rangle \approx 45\%$. The unit may be composed of small ($a \approx 0.1\,\mu\mathrm{m}$) grains of iron–poor silicates and troilite ($\langle \gamma^2 \rangle_{\mathrm{med}} = 0.36$), alternatively, comparably large grains ($a \approx 0.5\,\mu\mathrm{m}$) of any composition.

• *Unit 4.* Thick layers terrain with comparatively high reddening, $\langle R \rangle = 3.6\,\%\,\mathrm{k\AA}^{-1}$. Roughness and thermal inertia uncertain, possibly $\langle X \rangle \approx 0.26$, $\langle \xi \rangle = 0.75$ (e.g., 93% coverage of $S = 1.5$ pits), and $\langle \mathcal{I} \rangle \approx 2400\,\mathrm{J\,m^{-2}\,K^{-1}\,s^{-1/2}}$, corresponding to a porosity $\langle \psi \rangle \approx 35\%$. The unit may be composed of small ($a \approx 0.1\,\mu\mathrm{m}$) grains of iron–rich silicates and carbon ($\langle \gamma^2 \rangle_{\mathrm{med}} = 1$).

• *Unit 5.* Thin layers terrain with average reddening, $\langle R \rangle = 3.5\,\%\,\mathrm{k\AA}^{-1}$. Internal variations in R exist, which appear to correlate with previously identified layers (Belton *et al.* 2007). Roughness and thermal inertia uncertain, possibly rather smooth with $\langle X \rangle \approx 0.76$, $\langle \xi \rangle = 0.23$ (e.g., 62% coverage of $S = 0.4$ pits), and $\langle \mathcal{I} \rangle \approx 60\,\mathrm{J\,m^{-2}\,K^{-1}\,s^{-1/2}}$, corresponding to a porosity $\langle \psi \rangle \approx 85\%$. The unit may be composed of small ($a \approx 0.1\,\mu\mathrm{m}$) grains of iron–rich silicates and carbon ($\langle \gamma^2 \rangle_{\mathrm{med}} = 1$).

• *Unit 6.* Smooth terrain with comparatively high reddening, $\langle R \rangle = 3.6\,\%\,\mathrm{k\AA}^{-1}$. Rougness and thermal inertia uncertain, possibly $\langle X \rangle \approx 0.39$, $\langle \xi \rangle = 0.61$ (e.g., 87% coverage of $S = 1.2$ pits), and $\langle \mathcal{I} \rangle \approx 40\,\mathrm{J\,m^{-2}\,K^{-1}\,s^{-1/2}}$, corresponding to a porosity $\langle \psi \rangle \approx 85\%$. The unit may be composed

of small ($a \approx 0.1\,\mu$m) grains of iron–rich silicates and carbon ($\langle\gamma^2\rangle_{\rm med} = 1$).

• *Unit 7 North* ($l_{\rm co} \lesssim 125°$). Scarped/pitted terrain with comparatively high reddening, $\langle R\rangle = 3.6\,\%\,{\rm k\AA}^{-1}$. Rather smooth surface with $\langle X\rangle \approx 0.67$ and $\langle\xi\rangle \approx 0.33$ (e.g., 74% coverage of $S = 0.5$ pits). Modest thermal inertia around $\langle\mathcal{I}\rangle \approx 380\,{\rm J\,m^{-2}\,K^{-1}\,s^{-1/2}}$, corresponding to a porosity $\langle\psi\rangle \approx 70\%$. The unit may be composed of small ($a \approx 0.1\,\mu$m) grains of iron–rich silicates and carbon ($\langle\gamma^2\rangle_{\rm med} = 1$).

• *Unit 7 South* ($l_{\rm co} \gtrsim 125°$). Scarped/pitted terrain with comparatively high reddening, $\langle R\rangle = 3.6\,\%\,{\rm k\AA}^{-1}$. Rough surface with $\langle X\rangle \approx 0.26$ and $\langle\xi\rangle \approx 0.75$ (e.g., 91% coverage of $S = 1.6$ pits). Modest thermal inertia around $\langle\mathcal{I}\rangle \approx 1000\,{\rm J\,m^{-2}\,K^{-1}\,s^{-1/2}}$, corresponding to a porosity $\langle\psi\rangle \approx 60\%$. The unit may be composed of small ($a \approx 0.1\,\mu$m) grains of iron–poor silicates and troilite ($\langle\gamma^2\rangle_{\rm med} = 0.81$), alternatively, comparably large grains ($a \approx 0.5\,\mu$m) of any composition.

Judging from these results it appears that Comet 9P/Tempel 1 not only has a morphologically complex surface, but also that the physical properties differ between morphological units. These differences may be the result of evolutionary processes caused by e.g. sublimation, or could reflect a high degree of diversity among the cometesimals that once built this body – or both.

Units 3 and the southern part of unit 7 are particularly interesting due to their low volume emissivity factors which imply a peculiar surface composition and/or grain size distribution. Admittedly, this interpretation relies on the assumption that our numerical beaming function and the applied directional emissivity (i.e., $X'_{\rm mod}$) handle the dependence of the thermal emission flux on roughness as well as viewing and illumination geometry sufficiently well. In this context, it is interesting to note that the northern part of unit 1 and the southern part of unit 7 are illuminated at virtually the same incidence angle, and are viewed at virtually the same emission angle. According to the thermophysical modeling, the degree of roughness is higher for the southern part of unit 7 than for unit 1 but the difference is not dramatic. The only obvious reason for the difference in X' seen for these two parts of the surface is then compositional differences. This observation strengthens the idea of significant variations in composition and/or grain size, which is *independent* of the assumed numerical beaming function.

Substantial fractions of unit 3 are observed at very small emission angles $e \lesssim 10°$–$20°$, i.e., the DI line–of–sight is virtually along the local surface normal. Could this peculiar viewing geometry be responsible for the unusually low X' values associated with the unit, regardless of its composition? Should this be the case, it still does not explain the fact that the southern part of unit 7 has a similarly low X' even though it is observed at substantially higher emission angles, $e \gtrsim 60°$. Since both areas have very similar incidence angles, we do not see strong reasons to doubt that low X' values indeed are related to composition and/or grain size.

It is intriguing that unit 3 and parts of unit 7 simultaneously have a peculiar global topography (scarped/pitted terrain) *and* peculiar composition and/or grain size. Could the two properties somehow be connected? For example, if the two units represent previously active areas, one could imagine that sublimation–driven surface evolution has produced a highly irregular surface with substantial roughness on scales of decimeters to hundreds of meters. For example, sublimation under a dust mantle could gradually have undermined the near–surface structure, leading to collapse and the formation of pits and depressions. This could lead to the observed global scale pitted appearance, as well as to sub–resolution roughness revealed by high ξ values, leading to self heating during daytime which yields the observed low X values. The gas drag forces from the same sublimation process could have depleted the surface grain mixture of small grains, only leaving the larger grains behind. This could explain the observed low γ^2–values.

Alternatively, the suspected compositional and global scale structural properties of units 3 and the southern parts of unit 7 could be primordial. For example, one can imagine that the cometesimals forming these areas, in a talps–model scenario (Belton *et al.* 2007), could have a peculiar composition and/or grain size distribution due to grain growth and agglomeration under special conditions in the Solar Nebula. This could then explain the relatively low γ^2 values seen for these units. As the cometesimals deformed and smeared out during collision with the forming Comet 9P/Tempel 1, one could imagine that this process behaved differently than in other cometesimal collisions (again due to differing microphysical conditions), resulting in a visibly different global topography. However, this is of course only speculation.

Another intriguing difference between units concerns thermal inertia and porosity. Admittedly, the evidence for a substantial surface variation in these parameters is not particularly strong, yet worth discussing. The areas with supposedly unusually low thermal inertia, perhaps caused by a higher than average porosity (units 5, 6 and the northern part of unit 7) do share some common physical properties – apart from being neighbors. The average reddening tends to be high, $\langle R \rangle = 3.5\text{–}3.6\,\%\,\mathrm{k\AA}^{-1}$, although internal variations in R do exist. All three areas have X' and γ^2 close to unity which could indicate presence of small grains with high absorptivity.

The simultaneous occurrence of a comparably high reddening and values of X' and γ^2 near unity is untypical for all regions where it has been relatively securely determined that the thermal inertia is high. One may therefore speculate that the particular combination of composition, grain sizes, and high porosity that give units 5, 6, and the northern part of unit 7 their low thermal inertia, also tend to make their 1.2–2.5 μm spectra fairly red, and their 3.0–3.6 μm X' values (product of beaming function and directional emissivity) fairly close to unity. However, one possible counter example is unit 4, which also is relatively red and has X' near unity, but probably has a low porosity and large thermal inertia. Hence, it does not appear that the supposedly high porosity of units 5, 6, and the northern part of unit 7 lead to any other easily recognizable unique features.

4.3 Modeling Issues and Concluding Remarks

Since our model neglects energy losses due to sublimation, it is important to investigate how this may affect our results. First assuming that the total water production rate of $\sim 8 \cdot 10^{27}\,\mathrm{molec\,s^{-1}}$ at perihelion (see Davidsson et al. 2007 and references therein) is the result of homogeneous outgassing from the entire $119\,\mathrm{km}^2$ nucleus surface, the energy consumption due to sublimation is $\sim 5\,\mathrm{J\,s^{-1}\,m^{-2}}$, applying a latent heat of $L = 2.65 \cdot 10^6\,\mathrm{J\,kg^{-1}}$ for water ice. This should be compared to the conducted energy flux in Eq. (8), which is the difference between absorbed and reemitted fluxes (in reality this residual must be shared between conduction and sublimation). With a conductive heat flux in excess of $50\,\mathrm{J\,s^{-1}\,m^{-2}}$ for 76% of our pixels (and an average flux

of $100\,\mathrm{J\,s^{-1}\,m^{-2}}$), the errors introduced by neglecting homogeneous sublimation are negligible. In case the sublimation is concentrated to a smaller area on the nucleus, the local energy consumption ($\sim 50\,\mathrm{J\,s^{-1}\,m^{-2}}$ if 10% of the surface is active) would admittedly cause problems for the particular region in question, while the remainder of the nucleus then lacks sublimation and poses no problem. We excluded unit 2 (containing ice detected by Sunshine et al. (2006)) from our investigation to reduce the risk that sublimation affects our results.

Another assumption made is that the parameters X and $\mathcal{I}$ are quasi–constant within each co–latitude slab for a particular morphological unit. In case there are systematic variations in roughness and thermal inertia along such slabs, the fitted parameters may be inaccurate. Considering e.g. the lower panel of Fig. 5 it is clear that some variations indeed take place within a morphological unit, in this cases as function of l_{co}. However, these changes appear small and gradual, at least for unit 3, and there is no obvious reason to suspect that the longitudinal behavior should be different. Hence we do not consider this assumption critical.

A future investigation that might shed more light on the physical properties of morphological units on Comet 9P/Tempel 1 would include facets so far rejected due to global self heating and shadowing problems. This would require an enormous modeling effort, since each facet then has its own individual illumination function, for which all combinations of X and $\mathcal{I}$ must be tested. The current approach is simpler, since a large number of facets share the same illumination function (same l_{co}), just being imaged at different local hours. This would make it possible to investigate unit 6 and the southern part of units 4 and 5 more thoroughly. Yet another interesting project would be to consider other scans than #9000036. Although one then could improve the spatial resolution, a complicating factor is that the entire nucleus is not imaged.

Finally, for future spacecraft missions we recommend to aim at temperature uncertainties of at most $\pm 3\,\mathrm{K}$, in order to disentangle small scale surface roughness and thermal inertia.

ACKNOWLEDGMENTS. The authors thank the *Deep Impact* Principal Investigator Michael F. A'Hearn and his entire team for making their calibrated HRI–IR data and shape model publicly

available at the NASA Planetary Data System node. Furthermore, the detailed and encouraging review reports by A'Hearn and an anonymous referee helped us improve the presentation of our results substantially, for which we are grateful. The authors thank Ola Karlsson for generously sharing his FITS–reading software, and Johan Warell for fruitful discussions. This research has been financed by the Swedish National Space Board (SNSB) contract 135/06:2 (Davidsson).

Appendix A

We here illustrate that parameter pairs $\{X', T\}$ can be reliably extracted from the thermal emission spectra $I_{\rm th}(\lambda)$, as described in Sec. 2.1. First, the scatter in $I_{\rm th}(\lambda)$ with respect to the selected best fits $I_\lambda(X', T)$ at $3.0 \leq \lambda \leq 3.6\,\mu$m is characterized in order to quantify the noise level of the empirical spectra, $s(\lambda) = |I_{\rm th}(\lambda) - I_\lambda|/I_\lambda$. The median value $\langle s(\lambda)\rangle_{\rm med}$ for individual spectra varies between 0.5%–5.2% across the nucleus disk, with an overall average of $\overline{\langle s(\lambda)\rangle}_{\rm med} = 1.5\%$ (80% of the spectra has $\langle s(\lambda)\rangle_{\rm med} < 2.4\%$). The mean value $\langle s(\lambda)\rangle_{\rm mean}$ for individual spectra varies between 1.0%–9.8% across the nucleus disk, with an overall average of $\overline{\langle s(\lambda)\rangle}_{\rm mean} = 2.0\%$ (80% of the spectra has $\langle s(\lambda)\rangle_{\rm mean} < 3.6\%$). Noise with characteristics similar to that found for 80% of the spectra can be generated as

$$N_\lambda = 1 + 0.04 N_{\rm r} \tag{A.1}$$

where $N_{\rm r} \in [-1, 1]$ are random real numbers drawn from a normal distribution (one random number for each considered wavelength bin). Therefore synthetic spectra with realistic noise for known pairs $\{X', T\}$ can be generated as

$$I_{\rm s}(\lambda) = \frac{X' N_\lambda}{\pi} B_\lambda(T), \tag{A.2}$$

constituting a simulated HRI–IR spectrum. One can then test whether the procedure used to analyze real HRI–IR spectra indeed manages to recover the known $\{X', T\}$ from the simulated spectra. About 1000 synthetic spectra were generated for various $\{X', T\}$ combinations spanning the entire relevant parameter space. It was found that the correct X'–values and temperatures

could be recovered rather well, with median errors $\{\Delta X', \Delta T\}_{\rm med} = \{0.05, 1.5\,{\rm K}\}$, and mean errors $\{\Delta X', \Delta T\}_{\rm mean} = \{0.05, 2.0\,{\rm K}\}$. Note that $\Delta X'$ corresponds to the applied X' resolution used during fitting. Large errors, here defined as $\Delta X' \geq 0.2$ and $\Delta T \geq 7\,{\rm K}$ occurred for 3.6% and 2.3% of the synthetic spectra, respectively. This test makes us confident that the fitted parameters $\{X', T\}$ typically should be highly accurate, although a small number of individual pixels may obtain inaccurate solutions.

Appendix B

We here derive Eq. (8), the thermophysical energy balance equation for a surface illuminated by solar light, which dissipates heat by solid state heat conduction and thermal reradiation into space, where the latter energy loss is corrected for small scale surface roughness.

Consider an illuminated macroscopically rough terrain that is similar in size to a nucleus model facet (see Sec. 2.2). Divide the terrain into $N_{\rm t}$ elements, small enough to be considered macroscopically flat. Following Lagerros (1997) the irradiation G_i of element i is the total incident energy flux on that element. The radiosity J_i is defined as the total energy flux that is scattered off or emitted from element i. The irradiation is then,

$$G_i = \frac{S_\odot}{r_{\rm h}^2}\mu_i + \sum_{j\neq i}^{N_{\rm t}} F_{ij} J_j, \tag{B.1}$$

where the first term constitutes direct solar irradiation ($S_\odot$, $r_{\rm h}$, and μ_i are the solar constant, heliocentric distance, and cosine of the incidence angle, respectively) and the second term constitutes flux arriving from neighboring elements. The view factors F_{ij} (Lagerros 1997) specify the fraction of the flux originating from element j that is incident on element i (see Eq. (C.1) and the related discussion for more details). Equation (B.1) therefore takes into account self illumination from all elements within the facet (but global self heating, i.e., between *different facets*, is ignored).

The radiosity is given by

$$J_i = AG_i + \overline{\varepsilon}_{\rm h}\sigma_{\rm SB}T^4, \tag{B.2}$$

where the first term is scattered flux (A is the bolometric Bond albedo, i.e., spectral Bond albedo

convolved with the Planck function and integrated over wavelength) and the second term is emitted flux ($\sigma_{\rm SB}$ is the Stefan–Boltzmann constant). Here, $\overline{\varepsilon}_{\rm h}$ is the integrated emissivity (i.e., the directional emissivity $\varepsilon_{\rm d}$ is integrated over solid angle for the upper hemisphere to obtain the hemispherical emissivity $\varepsilon_{\rm h}$, which then is convolved with the Planck function and integrated over wavelength, which yields $\overline{\varepsilon}_{\rm h}$). It is assumed that all elements i share the same $\overline{\varepsilon}_{\rm h}$ and temperature T (the facet is considered isothermal). Furthermore, it is assumed that $A \approx 1 - \overline{\varepsilon}_{\rm h}$, although the Kirchhoff law is not strictly valid for these wavelength–integrated quantities. However, the hemispherical emissivity for relevant comet analogue material is close to unity near the thermal $T \approx 300\,{\rm K}$ Wien peak at $\lambda \approx 10\,\mu{\rm m}$ (which leads to $\overline{\varepsilon}_{\rm h}$–values near unity). Simultaneously, the spectral Bond albedo of comet nuclei is very low near the thermal $T \approx 5700\,{\rm K}$ Wien peak at $\lambda \approx 0.5\,\mu{\rm m}$ (which leads to A–values close to zero). Hence, $A \approx 1 - \overline{\varepsilon}_{\rm h}$ is a very reasonable assumption.

Assuming that all other energy sinks are negligible (e.g., ignoring sublimation), the difference between irradiance and radiosity is the heat flux flowing into the nucleus, i.e.,

$$\begin{aligned} -\kappa_i \frac{\partial T}{\partial x}\Big|_i &= G_i - J_i \\ &= (1-A)G_i - \overline{\varepsilon}_{\rm h}\sigma_{\rm SB}T^4 \\ &= (1-A)\left(\frac{S_\odot}{r_{\rm h}^2}\mu_i + \sum_{j\neq i}^{N_{\rm t}} F_{ij}\Big\{AG_j + \overline{\varepsilon}_{\rm h}\sigma_{\rm SB}T^4\Big\}\right) - \overline{\varepsilon}_{\rm h}\sigma_{\rm SB}T^4, \end{aligned} \tag{B.3}$$

where κ_i is the conductivity of element i.

Assuming that self heating is dominated by thermal emission rather than scattered light ($AG_j \ll \overline{\varepsilon}_{\rm h}\sigma_{\rm SB}T^4$ in the curled bracket), and that the conductivities and temperature gradients are similar for all elements, we calculate the average flux balance for the terrain by summing the fluxes for the elements (weighted by their surface areas s_i) and dividing with the total integrated rough area, obtaining for the terrain as a whole,

$$\frac{S_\odot(1-A)\mu}{r_{\rm h}^2} = \left(1 - \overline{\varepsilon}_{\rm h}\frac{\sum_i^{N_{\rm t}}\sum_{j\neq i}^{N_{\rm t}} F_{ij}s_i}{\sum_i^{N_{\rm t}} s_i}\right)\overline{\varepsilon}_{\rm h}\sigma_{\rm SB}T^4 - \kappa\frac{\partial T}{\partial x}, \tag{B.4}$$

where μ is the average (cosine of the) incidence angle for the terrain and κ is the average conductivity.

Since the small scale self heating parameter ξ is given by (Lagerros 1997),

$$\xi = \frac{\sum_i^{N_\mathrm{t}} \sum_{j \neq i}^{N_\mathrm{t}} F_{ij} s_i}{\sum_i^{N_\mathrm{t}} s_i}, \tag{B.5}$$

we have,

$$\frac{S_\odot (1-A) \mu}{r_\mathrm{h}^2} = (1 - \overline{\varepsilon}_\mathrm{h} \xi) \, \overline{\varepsilon}_\mathrm{h} \sigma_\mathrm{SB} T^4 - \kappa \frac{\partial T}{\partial x}. \tag{B.6}$$

Equation (8) follows by inserting Eqs. (7) and (9) into Eq. (B.6), applying the definition of thermal inertia ($\mathcal{I} = \sqrt{\rho C \kappa}$) and replacing μ by $\max\{\mu, 0\}$ to account for nighttime conditions.

Appendix C

Equation (10) assumes that shadowing and global (i.e., inter–facet) self heating due to nucleus topography is negligible. Since this assumption certainly is not true for many facets, these need to be identified and excluded in order not to compromise the applicability of the thermophysical model.

Hence, the incident solar flux is calculated for each facet versus time during a full rotation, taking shadowing by global topography into account. Facets that experience an integrated flux loss in excess of 5% (with respect to the integrated flux when shadowing is ignored) are excluded. To evaluate global self heating (i.e., scattered and reradiated flux from a facet j illuminating another facet i), view factors (Lagerros 1997) are calculated,

$$F_{ij} = \frac{\cos e_i \cos e_j}{\pi r^2} s_j, \tag{C.1}$$

where facet i is at emission angle e_j seen from j, where facet j is at incidence angle e_i seen from i, where r is the distance between the facets, and s_j is the surface area of facet j. An approximate total global self heating flux reaching facet i is then obtained as

$$H_i(t) = \sum_j F_{ij} \frac{S_\odot \mu_j(t)}{r_\mathrm{h}^2}, \tag{C.2}$$

where it is assumed that all solar flux reaching facet j is scattered and reemitted (i.e., no conduction into the interior), and where $\mu_j(t)$ is zero in case facet j is not illuminated (local nighttime or shadowing prevails), otherwise given by Eq. (10). Facets for which the global self heating flux exceeds 1% of the direct solar illumination flux during any time of the day are removed. Out of the 17225 facets nominally in the HRI–IR field of view, 5181 are not directly illuminated at the time of scan #9000036 (in 158 cases due to shadowing). Out of the remaining 12044 facets (constituting the illuminated part of the nucleus), 2321 are removed due to shadowing problems, and 585 are removed due to global self heating problems. Hence, 9138 facets remain and are the only ones considered in this study.

Appendix D

A beaming function consistent with the circular paraboloid pit model of surface roughness is obtained by first considering a single pit. Let $I_{\rm pit}(S, \mu_{\rm e}, \gamma)$ be the total intensity emitted at emission angle e (measured from the paraboloid symmetry axis, and $\mu_{\rm e} = \cos e$) from a circular paraboloid pit characterized by S. Let $I_{\rm rim}(\mu_{\rm e}, \gamma)$ be the total intensity emitted along the same $\mu_{\rm e}$ from a flat surface of area $A_{\rm rim}$. Then the beaming function for a single pit is given by,

$$\Lambda_*(S,\, \mu_{\rm e},\, \gamma) = \frac{I_{\rm pit}(S, \mu_{\rm e}, \gamma)}{I_{\rm rim}(\mu_{\rm e}, \gamma)}. \tag{D.1}$$

For the flat surface,

$$I_{\rm rim}(\mu_{\rm e}, \gamma) = 64\pi S^2 \mu_{\rm e} \varepsilon_{\rm d}(\mu_{\rm e},\, \gamma) \frac{1}{\pi} B_\lambda(T), \tag{D.2}$$

where the directional emissivity here is given by Eq. (21).

$I_{\rm pit}(S, \mu_{\rm e}, \gamma)$ is evaluated numerically by dividing the pit interior into a large number of (locally flat) facets i with surface areas s_i, temperatures T_i, cosine of emission angles $\mu_{{\rm e},i}$,

$$I_{\rm pit}(S, \mu_{\rm e}, \gamma) = \sum_i v_i s_i \varepsilon_{\rm d}(\mu_{{\rm e},i},\, \gamma) \mu_{{\rm e},i} \frac{1}{\pi} B_\lambda(T_i), \tag{D.3}$$

where $v_i = 0$ if a certain facet is not visible to an observer at $\mu_{\rm e}$. By assuming that the pit interior is isothermal at $T_i = T$ we obtain a beaming function consistent with Eq. (2), i.e., it should only

measure the change in intensity (with respect to a flat surface of the same temperature) caused by introducing macroscopic roughness. The existence of isothermal pits is an idealization, but is increasingly likely if the pits are physically small and if the thermal inertia is sufficiently large.

The beaming function for a terrain having a fraction f of its surface containing pits (while the remainder is flat) is then given by

$$\Lambda(S,\, f,\, \mu_{\rm e},\, \gamma) = 1 - f + f\Lambda_*(S,\, \mu_{\rm e},\, \gamma). \tag{D.4}$$

In the numerical calculation of Eq. (D.4), we considered $0.1 \leq S \leq 4.0$ with 0.1 resolution, $0.05 \leq \mu_{\rm e} \leq 1.00$ with 0.05 resolution, $0.05 \leq \gamma \leq 1.00$ with 0.05 resolution, while $0 \leq f \leq 1$ is any real number.

References

A'Hearn, M. F., and 32 colleagues, 2005. Deep Impact: Excavating Comet Tempel 1. Science 258, 258–264.

Belton, M. J. S., Thomas, P. C., Carcich, B., Crockett, C. J., and The Deep Impact Science Team, 2006. The spin state of 9P/Tempel 1. Lunar Planet. Sci. XXXVII, 1487.

Belton, M. J. S., and 13 colleagues, 2007. The internal structure of Jupiter family cometary nuclei from Deep Impact observation: The talps or "layered pile" model. Icarus 187, 332–344.

Belton, M. J. S., Melosh, H. J., 2008. Smooth terrain on Comet Tempel 1: A gas–fluidized landslide. AAS/Division for Planetary Sciences Meeting Abstracts 40, 02.06.

Blum, J., Schräpler, R., Davidsson, B. J. R., Trigo-Rodríguez, J. M., 2006. The physics of protoplanetesimal dust agglomerates. I. Mechanical properties and relations to primitive bodies in the Solar System. Astron. J. 652, 1768–1781.

Bohren, C. F., and Huffman, D. R., 1983. Absorption and scattering of light by small particles. John Wiley & Sons, Inc., New York.

Cord, A. M., Pinet, P. C., Daydou, Y., Chevrel, S. D., 2003. Planetary regolith surface analogs: optimized determination of Hapke parameters using multi–angular spectro–imaging laboratory data. Icarus 165, 414–427.

Davidsson, B. J. R., 2006. The bulk density of cometary nuclei. In: Ip, W.-H., Bhardwaj, A. (Eds.), Advances in Geosciences, Vol. 3, Planetary Science, World Scientific, Singapore, pp. 155–169.

Davidsson, B. J. R., Gutiérrez, P. J., Rickman, H., 2007. Nucleus properties of Comet 9P/Tempel 1 estimated from non–gravitational force modeling. Icarus 187, 306–320.

Dorschner, J., Begemann, B., Henning, T., Jäger, C., Mutschke, H., 1995. Steps toward interstellar silicate mineralogy. II. Study of Mg–Fe–silicate glasses of variable composition. Astron. Astrophys. 300, 503–520.

Ernst, C. M., Schultz, P. H., 2007. Evolution of the Deep Impact flash: Implications for the nucleus surface based on laboratory experiments. Icarus 190, 334–344.

Groussin, O., Lamy, P., Jorda, L., 2004. Properties of the nuclei of Centaurs Chiron and Chariklo. Astron. Astrophys. 413, 1163–1175.

Groussin, O., A'Hearn, M. F., Li, J.-Y., Thomas, P. C., Sunshine, J. M., Lisse, C. M., Meech, K. J., Farnham, T. L., Feaga, L. M., Delamere, W. A., 2007. Surface temperature of the nucleus of Comet 9P/Tempel 1. Icarus 187, 16–25.

Hampton, D. L., Baer, J. W., Huisjen, M. A., Varner, C. C., Delamere, A., Wellnitz, D. D., A'Hearn, M. F., Klaasen, K. P., 2005. An overview of the instrument suite for the Deep Impact mission. Space Sci. Rev. 117, 43–93.

Hansen, O. L., 1977. An explication of the radiometric method for size and albedo determination. Icarus 31, 456–482.

Hapke, B., 1984. Bidirectional reflectance spectroscopy. 3. Correction for macroscopic roughness. Icarus 59, 41–59.

Hapke, B., 1993. Theory of reflectance and emittance spectroscopy. Cambridge University Press.

Harmon, J. K., Nolan, M. C., Ostro, S. J., Campbell, D. B., 2004. Radar studies of comet nuclei and grain comae. In: Festou, M. C., Keller, H. U., Weaver, H. A. (Eds.), Comets II, Univ. of Arizona Press, Tucson, pp. 265–279.

Harmon, J. K., Nolan, M. C., Howell, E. S., Giorgini, J. D., 2008. Comet 8P/Tuttle: Arecibo radar observations of the first bilobate comet. In: Asteroids, Comets, Meteors 2008, Abstract #8025. Lunar and Planetary Institute, Houston. CD–ROM.

Harris, A. W., Mueller, M., Delbó, M., Bus, S. J., 2005. The surface properties of small asteroids: Peculiar Betulia – A case study. Icarus 179, 95–108.

Harris, A. W., Mueller, M., Delbó, M., Bus, S. J., 2007. Physical characterization of the potentially hazardous high–albedo Asteroid (33342) 1998 WT_{24} from thermal–infrared observations. Icarus 188, 414–424.

Helfenstein, P., 1988. The geological interpretation of photometric surface roughness. Icarus 73, 462–481.

Helfenstein, P., Shepard, M. K., 1999. Submillimeter–scale topography of the Lunar regolith. Icarus 141, 107–131.

Horai, K.-I., 1971. Thermal conductivity of rock–forming minerals. J. Geophys. Res. 76(5), 1278–1308.

Jäger, C., Mutschke, H., Henning, T., 1998. Optical properties of carbonaceous dust analogues. Astron. Astrophys. 332, 291–299.

Jorda, L., Lamy, P., Faury, G., Keller, H. U., Hviid, S., Küppers, M., Koschny, D., Lecacheux, J., Gutiérrez, P., Lara, L. M., 2007. Properties of the dust cloud caused by the Deep Impact experiment. Icarus 187(1), 208–219.

Kömle, N. I., Kargl, G., Thiel, K., Seiferlin, K., 1996. Thermal properties of cometary ices and sublimation residua including organics. Planet. Space Sci. 44(7), 675–689.

Lagerros, J. S. V., 1997. Thermal physics of asteroids. III. Irregular shapes and albedo variegations. Astron. Astrophys. 325, 1226–1236.

Lebofsky, L. A., Spencer, J. R., 1989. Radiometry and thermal modeling of asteroids. In: Binzel, R. P., Gehrels, T., Matthews, M. S. (Eds.), Asteroids II, The University of Arizona Press, Tucson, pp. 128–147.

Li, J.-Y., and 10 colleagues, 2007. Deep Impact photometry of Comet 9P/Tempel 1. Icarus 187, 41–55.

Lisse, C. M., Kraemer, K. E., Nuth III, J. A., Li, A., Joswiak, D., 2007. Comparison of the composition of the Tempel 1 ejecta to the dust in Comet C/Hale–Bopp 1995 O1 and YSO HD 100546. Icarus 187, 69–86.

Mueller, M., Delbó, M., di Martino, M., Harris, A. W., Kaasalainen, M., Bus, S. J., 2007. Indications for regolith on Itokawa from thermal–infrared observations. ASP Conference Series. In press.

Müller, M. 2007. Surface properties of asteroids from mid–infrared observations and thermophysical modeling. Universitätsbibliothek der Freien Universität Berlin, Berlin. PhD Thesis, http://www.diss.fu–berlin.de/diss/receive/FUDISS_thesis_000000002596.

Müller, T. G., Sterzik, M. F., Schütz, O., Pravec, P., Siebenmorgen, R., 2004. Thermal infrared observations of near–Earth asteroid 2002 NY40. Astron. Astrophys. 424, 1075–1080.

Müller, T. G., Sekiguchi, T., Kaasalainen, M., Abe, M., Hasegawa, S., 2005. Thermal infrared observations of the Hayabusa spacecraft target asteroid 25143 Itokawa. Astron. Astrophys. 443, 347–355.

Pollack, J. B., Hollenbach, D., Beckwith, S., Simonelli, D. P., Roush, T., Fong., W., 1994. Composition and radiative properties of grains in molecular clouds and accretion disks. Astrophys. J. 421, 615–639.

Press, W. H., Flannery, B. P., Teukolsky, S. A., Vetterling, W. T., 1986. Numerical Recipes.

The Art of Scientific Computing. Cambridge University Press, Cambridge.

Richardson, J. E., Melosh, H. J., Lisse, C. M., Carcich, B., 2007. A ballistic analysis of the Deep Impact ejecta plume: Determining Comet Tempel 1's gravity, mass, and density. Icarus 190(2), 357–390.

Richet, P., Robie, R. A., Hemingway, B. S., 1993. Entropy and structure of silicate glasses and melts. Geochimica et Cosmochimica Acta 57, 2751–2766.

Robie, R. A., Hemingway, B. S., Takei, H., 1982. Heat capacities and entropies of Mg_2SiO_4, Mn_2SiO_4, and Co_2SiO_4 between 5 K and 380 K. American Mineralogist 67, 470–482.

Shepard, M. K., Campbell, B. A., 1998. Shadows on a planetary surface and implications for photometric roughness. Icarus 134, 279–291.

Shepard, M. K., Helfenstein, P., 2007. A test of the Hapke photometric model. J. Geophys. Res. 112, 3001–3017.

Shoshany, Y., Prialnik, D., Podolak, M., 2002. Monte Carlo modeling of the thermal conductivity of porous cometary ice. Icarus 157, 219–227.

Sunshine, J. M., and 22 colleagues, 2006. Exposed water ice deposits on the surface of comet Tempel 1. Science 311, 1453–1455.

Sunshine, J. M., Groussin, O., Schultz, P. H., A'Hearn, M. F., Feaga, L. M., Farnham, T. L., Klaasen, K. P., 2007. The distribution of water ice in the interior of Comet Tempel 1. Icarus 190, 284–294.

Thomas, P. C., and 14 colleagues, 2007. The shape, topography, and geology of Tempel 1 from Deep Impact observations. Icarus 187, 4–15.

Toon, O. B., Ackerman, T. P., 1981. Algorithms for the calculation of scattering by stratified spheres. Appl. Opt. 20, 3657–3660.

List of Parameters

Symbol	Description
a	Grain radius
A	Bolometric Bond albedo
A_{mod}	Modeled bolometric Bond albedo
A_{v}	Spectral Bond albedo integrated over V–band
A_{flat}	Projected flat area of rough terrain
A_{pit}	Integrated surface area of pit interior
A_{rim}	Pit opening area
A_{rough}	Surface area of rough terrain
$\mathcal{A}$	Mean slope angle distribution function parameter
b	Parameter in incomplete gamma function
$B_\lambda(T)$	Planck function
$\mathcal{B}$	Mean slope angle distribution function parameter
c	Speed of light in vacuum
C	Specific heat capacity
d	Distance from parabola focus to vertex
d_{co}	Co–declination
D	Mean slope angle distribution
e	Emission/incidence angle (depending on context)
f	Fraction of surface covered with pits
F_{ij}	View factor
G	Irradiation
h	Planck constant
H	Maximum distance (in time) for T_{emp} data points to local noon
H_{i}	Global self heating flux reaching facet j
$\mathcal{H}$	Range of local hours covered by T_{emp}
i	Index

Table 1: Description of all parameter symbols used in the paper.

Table 1 cont'd

$\mathcal{I}$	Thermal inertia of porous medium
$\mathcal{I}_{\rm comp}$	Thermal inertia of compacted medium
$I_{\rm DI}$	Spectral intensity from DI pipeline
$I_{\rm pit}$	Spectral intensity emitted by pit
$I_{\rm rim}$	Spectral intensity emitted by flat area of size $A_{\rm rim}$
$I_{\rm R}$	Spectral intensity of reddened sunlight
$I_{\rm s}$	Synthetic spectral intensity
$I_{\rm th}$	Spectral intensity of thermal emission
I_λ	Modeled spectral intensity
j	Index
J	Radiosity
k	Boltzmann constant
$l_{\rm co}$	Co–latitude
M	Number of data points in $T_{\rm emp}$ bin
$N_{\rm r}$	Random number
$N_{\rm t}$	Number of flat surface elements in rough terrain
N_λ	Synthetic noise function
p	Parameter in Φ function
P	Rotational period
Q	Incomplete gamma function
$Q_{\rm A}$	Absorption coefficient
$Q_{\rm E}$	Extinction coefficient
r	Distance between facets in shape model
$r_{\rm h}$	Heliocentric distance
R	Reddening
S	Pit depth–to–diameter ratio
$S_{\rm min}$	Smallest S consistent with estimated ξ

Table 1 cont'd

$S_\odot$	Solar constant
s	Noise in $I_{\rm th}$ relative to I_λ
$s_{\rm i}$	Surface area of element i
t	Time
t_0	Time of solar culmination
T	Temperature
ΔT	Temperature difference
$T_{\rm emp}$	Empirical temperature function
$\Delta T_{\rm emp}$	Empirical temperature function error bar
v_i	Pit interior visibility switch
w	Parameter in incomplete gamma function
x	Depth below comet surface
x_*	Dimensionless depth below comet surface
x'_*	Dimensionless thickness of modeled surface slab
X	Effective integrated emissivity
X'	Product $\Lambda\varepsilon_{\rm d}$
$\Delta X'$	Difference in X'
$X'_{\rm mod}$	Modeled version of X'
$X_\star$	Curve tracing low–χ^2 in $\{X, \mathcal{I}\}$ phase space
y	Silicate iron abundance parameter
α	Right ascension
γ^2	Volume emissivity factor
$\gamma^2_{\rm mod}$	Modeled volume emissivity factor
δ	Declination
$\varepsilon_{\rm d}$	Directional emissivity
$\varepsilon_{\rm h}$	Hemispherical emissivity
$\varepsilon_{\rm h,mod}$	Modeled hemispherical emissivity
$\overline{\varepsilon}_{\rm h}$	Integrated emissivity
$\overline{\varepsilon}_{\rm h,mod}$	Modeled integrated emissivity

Table 1 cont'd

θ	Angle between local surface normal and rough surface average normal
$\bar{\theta}_{\rm i}$	Input mean slope angle
$\bar{\theta}_{\rm o}$	Output mean slope angle
$\bar{\theta}$	Mean slope angle
κ	Conductivity of porous material
$\kappa_{\rm comp}$	Conductivity of compacted material
λ	Wavelength
$\Delta\lambda$	Wavelength bin
Λ	Beaming function
Λ_*	Beaming function of single pit
μ	Cosine of incidence angle
$\mu_{\rm e}$	Cosine of emission angle
ν	Number of degrees of freedom
ξ	Small scale self heating parameter
ρ	Density of porous material
$\rho_{\rm bulk}$	Bulk density of the entire comet nucleus
$\rho_{\rm comp}$	Density of compacted material
σ	Standard deviation
$\sigma_{\rm SB}$	Stefan–Boltzmann constant
Φ	Ratio $\kappa/\kappa_{\rm comp}$
χ^2	Temperature chi–square
$\chi^2_{\rm R}$	Reddening chi–square proxy
$\chi^2_{\rm th}$	Near–infrared thermal emission chi–square proxy
ψ	Porosity
ω	Rotational angular frequency

Fixed Thermophysical Model Parameters

Parameter	Symbol	Value
Heliocentric distance	$r_{\rm h}$	1.5062 AU
Co–declination	$d_{\rm co}$	80.827°
Rotational period	P	40.7 h
Bolometric Bond albedo	A	0.013
Integrated emissivity	$\overline{\varepsilon}_{\rm h}$	0.987

Table 2: The heliocentric distance $r_{\rm h}$ is valid at the time of scan #9000036. The co–declination $d_{\rm co}$ follows from the orbital position and the positive spin pole in the equatorial system $\{\alpha, \delta\} = \{293°.8, 72°.6\}$ (with an uncertainty of 5°) obtained by Thomas *et al.* (2007). The rotational period P was measured by Belton *et al.* (2006). The spectral Bond albedo integrated over the V–band is $A_{\rm v} = 0.013 \pm 0.002$ according to Li *et al.* (2007). The difference between the bolometric albedo A and $A_{\rm v}$ is typically less than 10% (Hansen 1977), i.e., comparable to the error bars in $A_{\rm v}$. Hence we take $A = 0.013$ and the listed $\overline{\varepsilon}_{\rm h}$ follows from $\overline{\varepsilon}_{\rm h} \approx 1 - A$ (see Appendix B).

FIG. 1 Spectrum $\{16, 130\}$ from the 40×256 HRI–IR scan #9000036. The upper left panel shows the spectrum after bad pixel removal. The upper right panel shows a reddened ($R = 2.8\,\%\,\mathrm{k\AA}^{-1}$) solar spectrum fitted to the $1.2 \leq \lambda \leq 2.5\,\mu$m region. The lower left panel shows the thermal spectrum remaining after removal of scattered solar light. The lower right panel shows a model fit to the thermal spectrum in the $3.0 \leq \lambda \leq 3.6\,\mu$m region (indistinguishable from the empirical spectrum at this scale) characterized by $\{X', T\} = \{0.7, 307.5\,\mathrm{K}\}$, see Eq. (4).

FIG. 2 Cartoon of morphological unit boundaries as defined by Thomas et al. (2007), drawn on top of image "hv0173727679_9000907_001_rr.jpg" from the PDS archive for context. The morphological units are here numbered from 1 through 7 as indicated.

FIG. 3 Upper left panel: spectral reddening R valid at $1.2 \leq \lambda \leq 2.5\,\mu$m. To increase the contrast, only pixels with $2.5 \leq R \leq 4.5\,\%\,\mathrm{k\AA}^{-1}$ are shown here. Upper right panel: $X' = \Lambda\varepsilon_\mathrm{d}$ valid at $3.0 \leq \lambda \leq 3.6\,\mu$m. Lower left panel: nucleus surface temperature. Lower right panel: volume emissivity factor γ^2 (note that black areas represent pixels removed due to shadowing and/or global self heating problems as well as presence of surface water ice).

FIG. 4 Upper panel: temperatures obtained from the analysis of HRI–IR spectra (T_emp) compared with three models with different $\{X, \mathit{\Gamma}\}$ and resulting χ^2– and Q–values. Lower panel: models in $\{X, \mathit{\Gamma}\}$ parameter space yielding solutions $T(t)$ statistically consistent with $T_\mathrm{emp}(t)$, using a $Q \geq 0.01$ criterion.

FIG. 5 Modeled X values versus co–latitude l_co for unit 1 (upper panel) and unit 3 (lower panel). Circles show $\min(\chi^2)$ solutions and error bars correspond to a 99% confidence level or roughly 3–σ (incomplete gamma function values $Q \geq 0.01$).

FIG. 6 Modeled X values versus co–latitude l_co for unit 4 (upper panel) and unit 5 (lower panel). Symbols show $\min(\chi^2)$ solutions and error bars correspond to a 99% confidence level or roughly 3–σ (incomplete gamma function values $Q \geq 0.01$). Circles and squares are used to distinguish

$X \geq 0.4$ and $X < 0.4$ cases, respectively.

FIG. 7 Examples of theoretical temperature curves $T = T(t)$ for three different $\{X, \mathcal{I}\}$ models.

FIG. 8 The $\min(\chi^2)$ solutions for X versus H (the maximum hour angle extension of the data set with respect to the solar culmination time), for unit 4 and 5.

FIG. 9 Modeled thermal inertia $\mathcal{I}$ versus co–latitude $l_{\rm co}$ for unit 1 (upper panel) and unit 3 (lower panel). Circles show $\min(\chi^2)$ solutions and error bars correspond to a 99% confidence level or roughly 3–σ (incomplete gamma function values $Q \geq 0.01$). Thermal inertia is given in units of $[\mathrm{J\,m^{-2}\,K^{-1}\,s^{-1/2}}]$.

FIG. 10 Upper panel: smallest depth–to–diameter ratio $S_{\rm min}$ consistent with the estimated small scale surface self heating parameter ξ according to the circular paraboloid model. Lower panel: the corresponding area coverage of pits in per cent.

FIG. 11 Modeled hemispherical emissivity $\varepsilon_{\rm h,mod}$ as function of wavelength for various grain radii a. The different panels show $\varepsilon_{\rm h,mod}$ for different substances, as indicated in the figure.

FIG. 12 Modeled volume emissivity factors $\gamma^2_{\rm mod}$ versus grain radius a at the wavelength $\lambda = 3.25\,\mu$m for a number of species, as indicated in the figure.

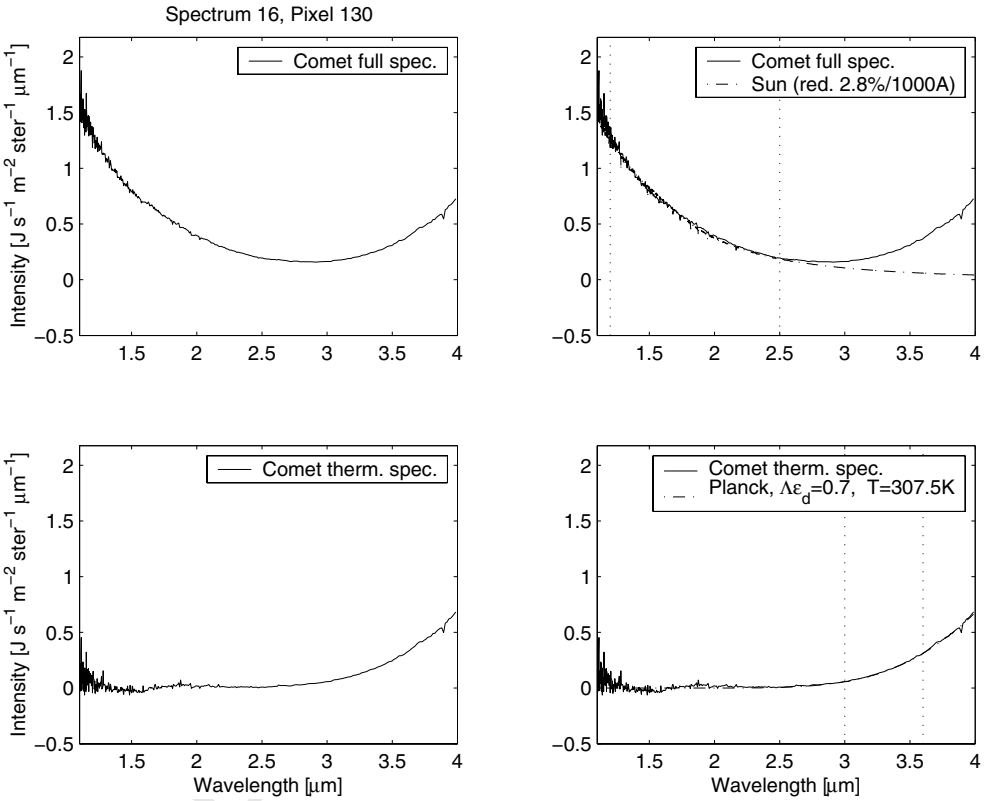

Figure 1: Björn J. R. Davidsson, Pedro J. Gutiérrez, Hans Rickman

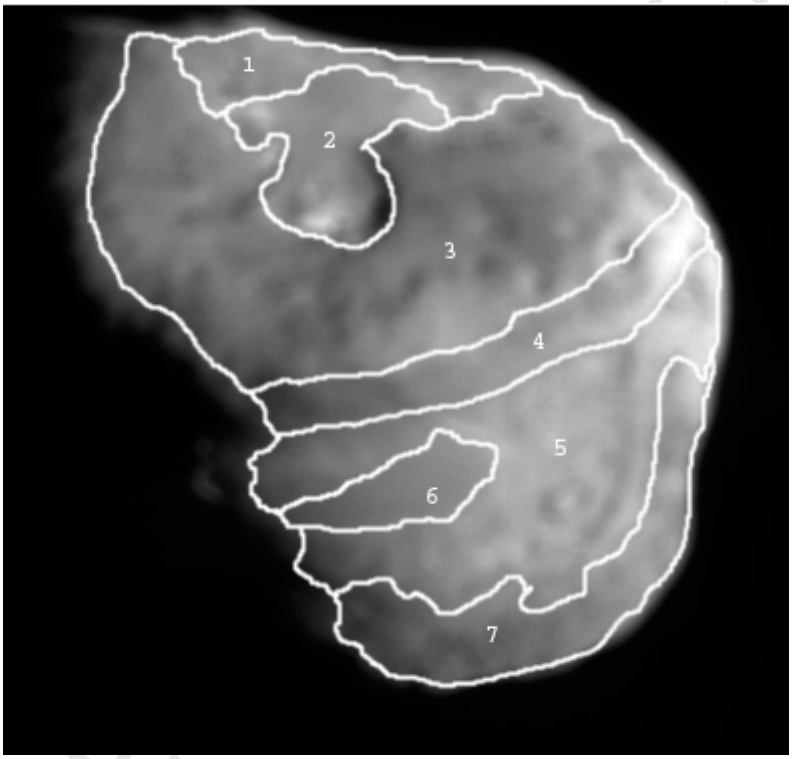

Figure 2: Björn J. R. Davidsson, Pedro J. Gutiérrez, Hans Rickman

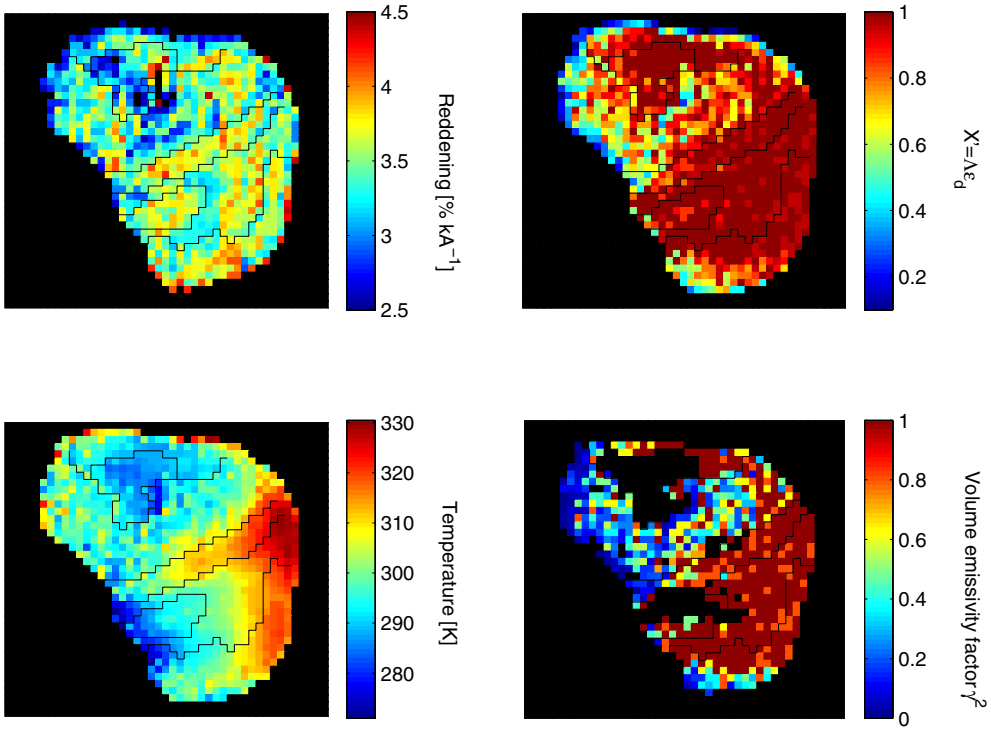

Figure 3: Björn J. R. Davidsson, Pedro J. Gutiérrez, Hans Rickman

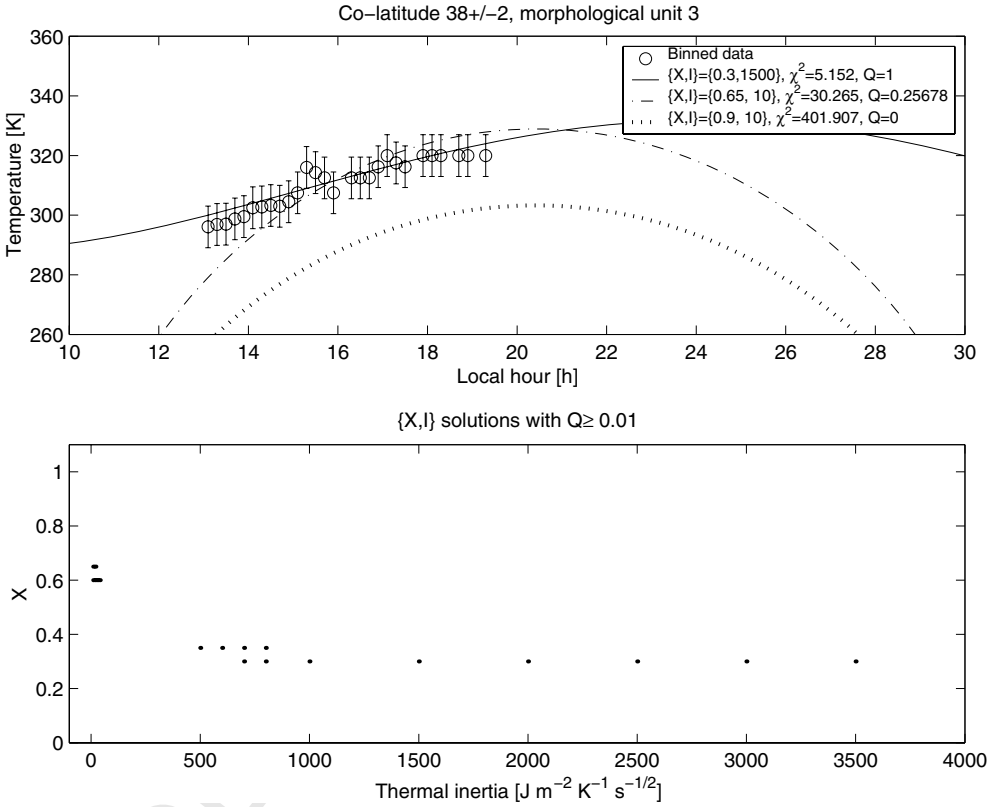

Figure 4: Björn J. R. Davidsson, Pedro J. Gutiérrez, Hans Rickman

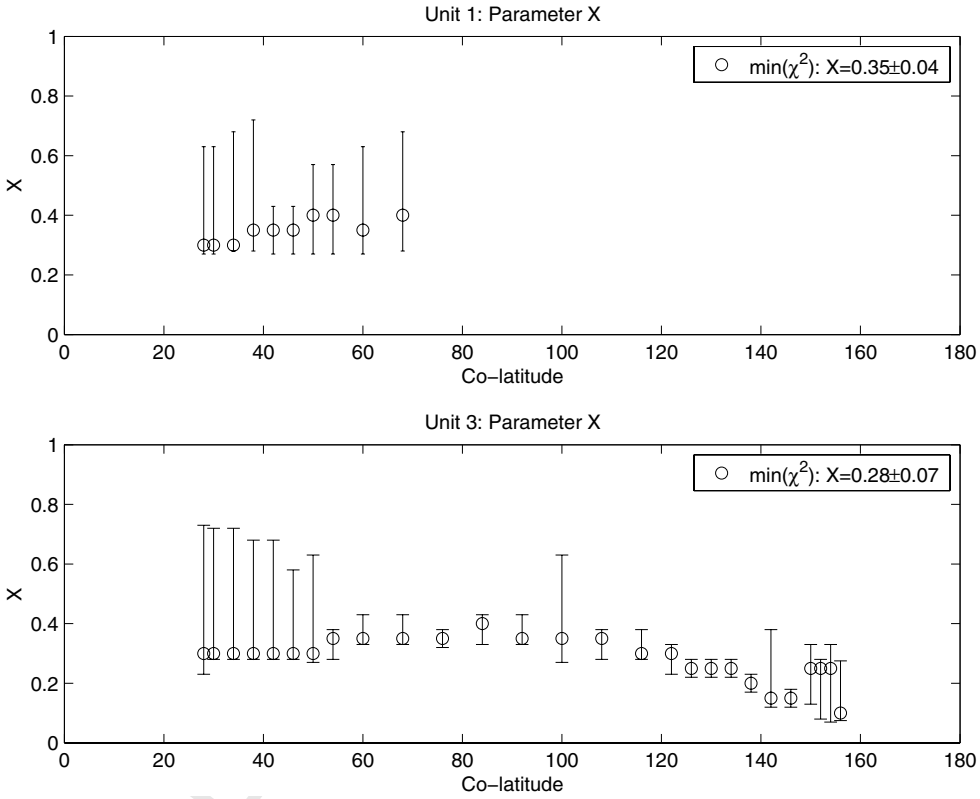

Figure 5: Björn J. R. Davidsson, Pedro J. Gutiérrez, Hans Rickman

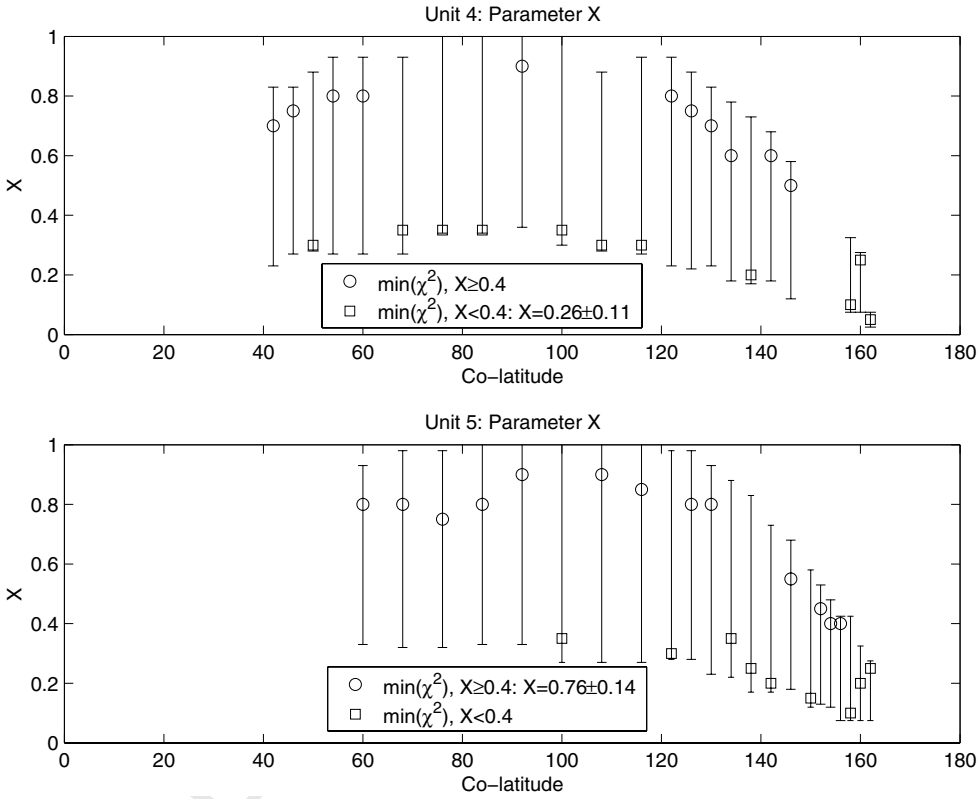

Figure 6: Björn J. R. Davidsson, Pedro J. Gutiérrez, Hans Rickman

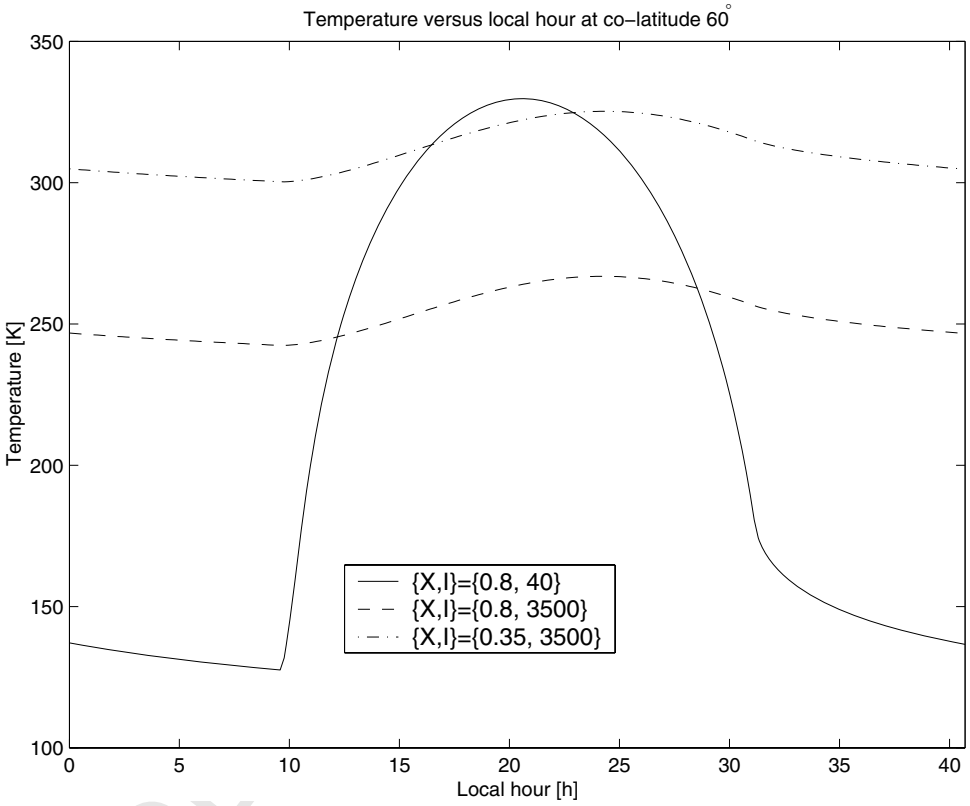

Figure 7: Björn J. R. Davidsson, Pedro J. Gutiérrez, Hans Rickman

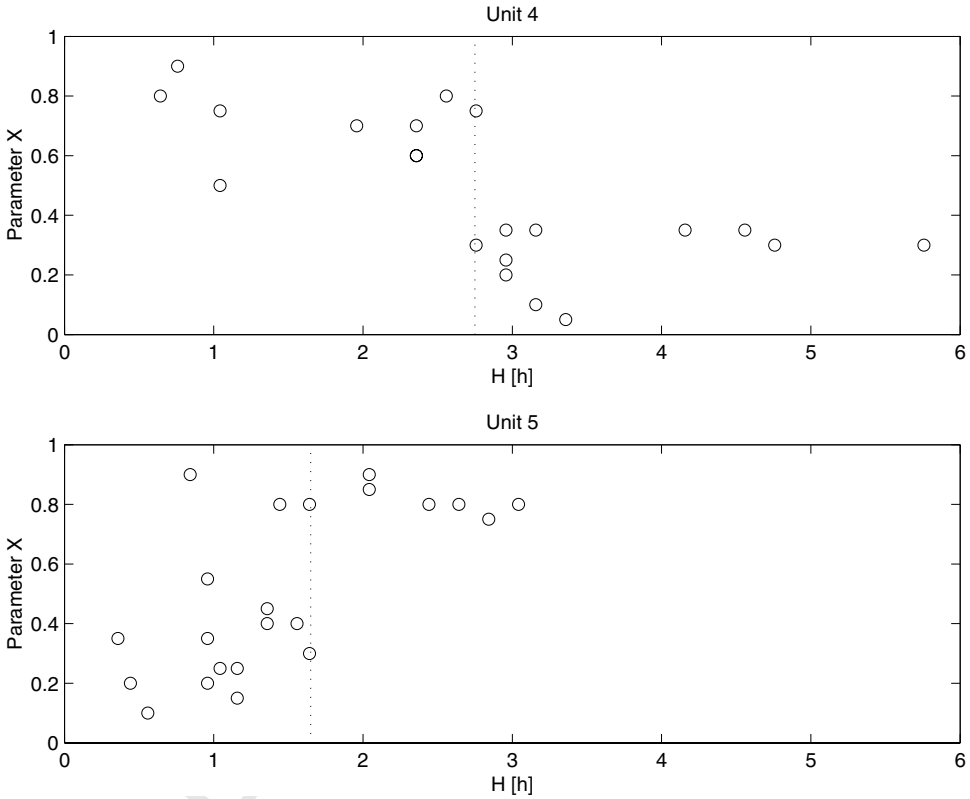

Figure 8: Björn J. R. Davidsson, Pedro J. Gutiérrez, Hans Rickman

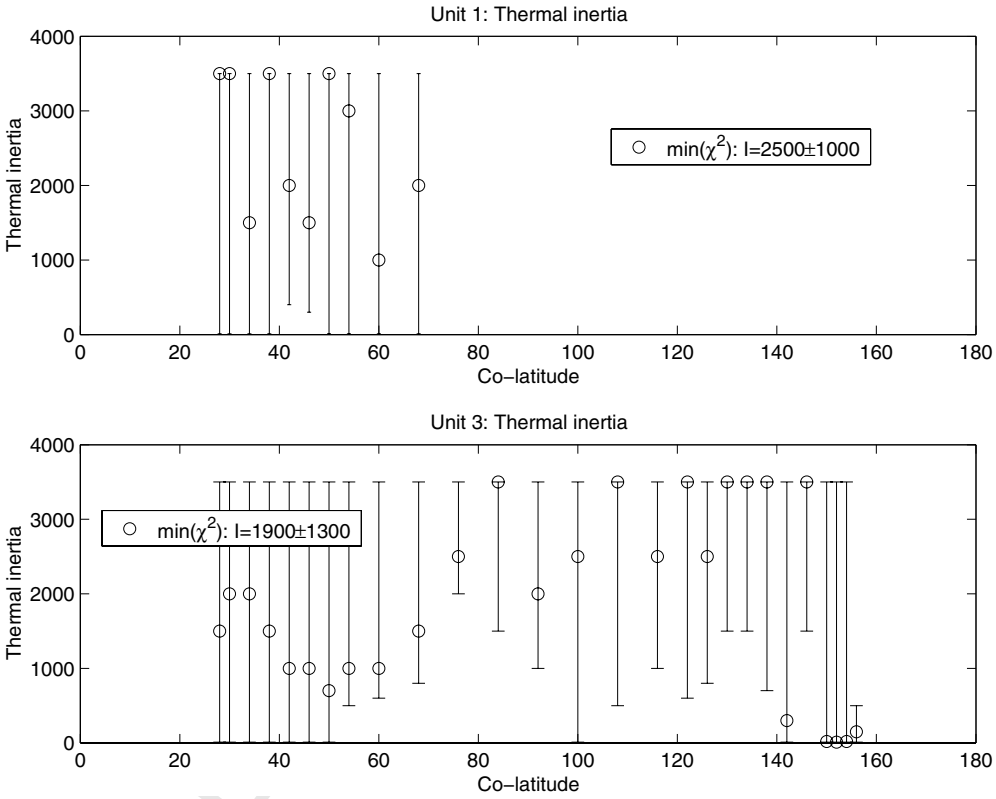

Figure 9: Björn J. R. Davidsson, Pedro J. Gutiérrez, Hans Rickman

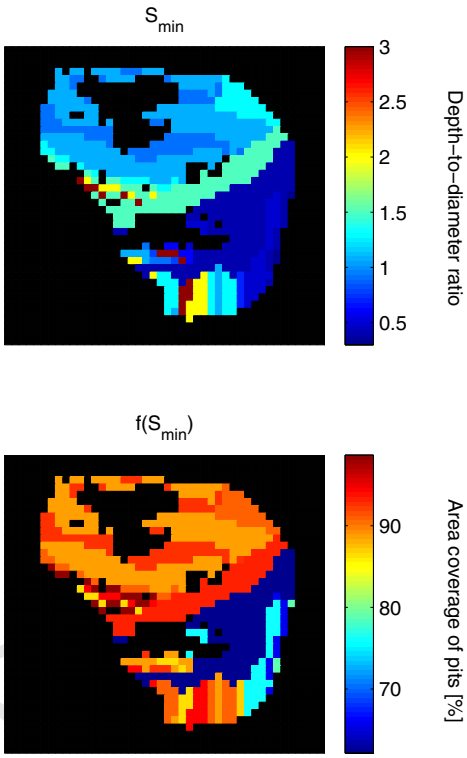

Figure 10: Björn J. R. Davidsson, Pedro J. Gutiérrez, Hans Rickman

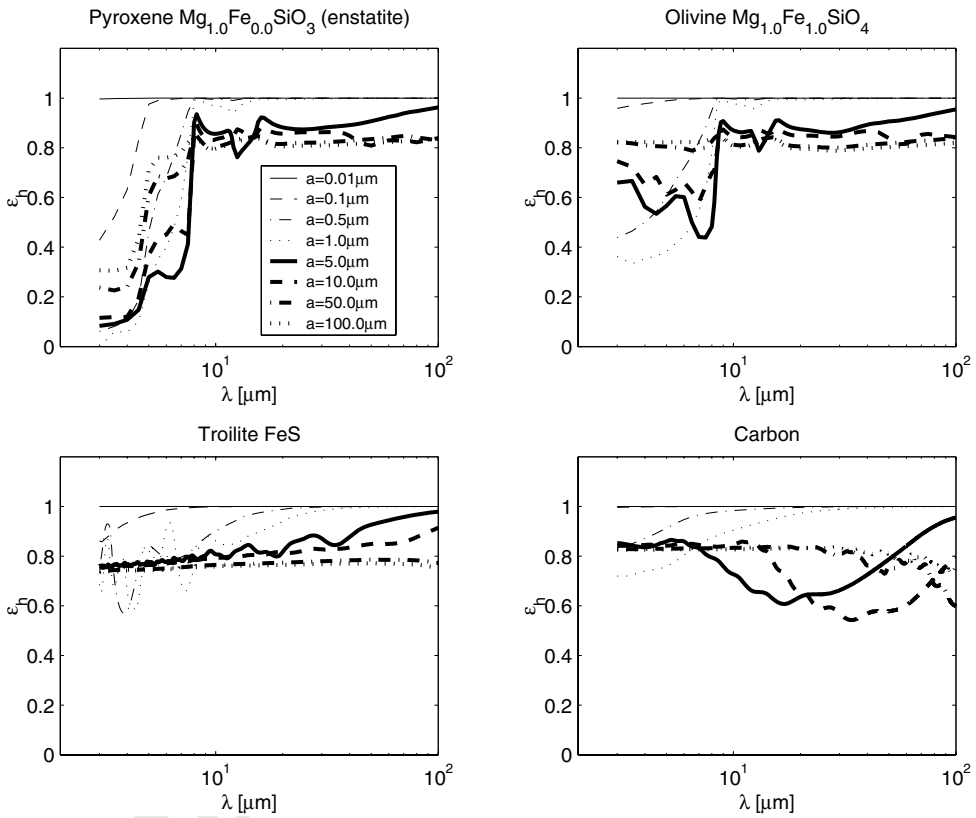

Figure 11: Björn J. R. Davidsson, Pedro J. Gutiérrez, Hans Rickman

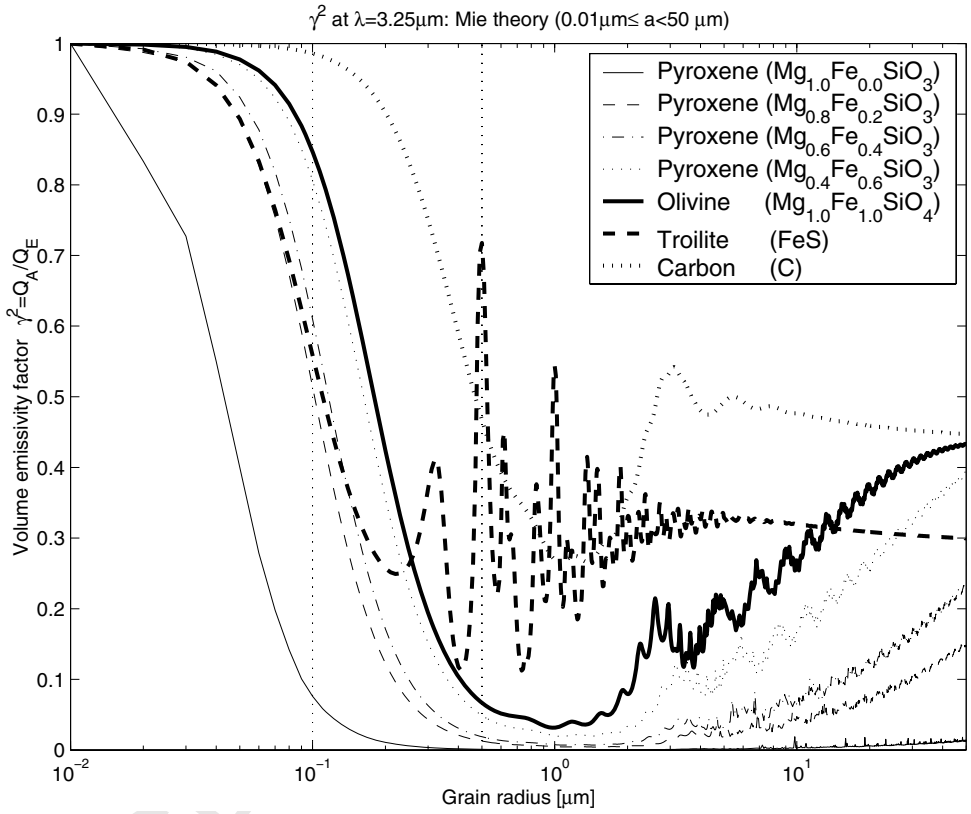

Figure 12: Björn J. R. Davidsson, Pedro J. Gutiérrez, Hans Rickman